Citation for final published version:

Starr, Aidan, Hall, Ian R. , Ninnemann, Ulysses S., Barker, Stephen , Charles, Christopher D., Nederbragt, Alexandra, Owen, Lindsey, Tangunan, Deborah and Zhang, Xu 2026. Southern ocean vertical carbon stratification across the Mid-Pleistocene Transition. Paleoceanography and Paleoclimatology 41 (3) , e2024PA005090. 10.1029/2024pa005090

Publishers page: https://doi.org/10.1029/2024pa005090

Southern Ocean vertical carbon stratification across the Mid-Pleistocene Transition

Aidan Starr[1,2]†[*], Ian R. Hall[2*], Ulysses S. Ninnemann[3], Stephen Barker[2], Christopher D. Charles[4], Alexandra Nederbragt[2], Lindsey Owen[2], Deborah Tangunan[2,5], Xu Zhang[6]

[1]Department of Geography, University of Cambridge, Cambridge, UK.
[2]School of Earth and Environmental Sciences, Cardiff University, Cardiff, UK.
[3]Department of Earth Science and Bjerknes Centre for Climate Research, University of Bergen, Bergen, Norway.
[4]Scripps Institution of Oceanography, University of California San Diego, CA, USA.
[5]Department of Earth Sciences, University College London, London, UK.
[6]British Antarctic Survey, Cambridge, UK.

*Corresponding author: Aidan Starr (ams332@cam.ac.uk); Ian R. Hall (Hall@cardiff.ac.uk)

†Now at Climate X, 31 Great Winchester Street, London.

Key Points:

- Breakdowns of Southern Ocean carbon isotope stratification occur at multiple glacial terminations back to at least 1.55 million years ago.
- An increasingly efficient Southern Ocean biological pump across the Mid-Pleistocene Transition may have played a role in decreasing glacial CO_2.
- Southern Ocean carbon isotope stratification maxima and atmospheric CO_2 minima become decoupled during Late Pleistocene glacials.

Abstract

Paleoceanographic evidence detailing the evolution of ocean carbon sequestration at high resolution across the Mid-Pleistocene Transition (MPT; 1.2–0.7 Ma, million years ago) remains scarce. Here, we present a continuous record of the stable carbon isotope gradient, referred to as the 'chemocline', between the sub-surface and deep ocean ($\Delta\delta^{13}C_{(sub\text{-}deep)}$) from a Subantarctic Zone (SAZ) sediment core site located south of Africa. We demonstrate that periodic breakdowns of Southern Ocean chemocline occur at multiple glacial terminations extending back to at least 1.55 Ma, coinciding with intensified upwelling in the Antarctic Zone (AAZ) (Jaccard et al., 2013). This indicates that the accumulation and (rapid) release of respired carbon from the deep Southern Ocean is a recurring feature of glacial-interglacial cycles in both the pre-MPT and post-MPT world. A comparison of $\Delta\delta^{13}C_{(sub\text{-}deep)}$ and records of atmospheric CO_2 levels and SAZ iron accumulation reveals a potential relationship between a more efficient Southern Ocean biological pump and declining glacial CO_2 levels across the Early to Middle Pleistocene. This apparent coupling breaks down after ~300 ka, wherein glacial $\Delta\delta^{13}C_{(sub\text{-}deep)}$ levels revert to pre-MPT levels, while glacial CO_2 remains low. One explanation is that an expansion of the SAZ during glacials between these two intervals modifies $\Delta\delta^{13}C_{(sub\text{-}deep)}$ at our study site without necessitating a change in CO_2 level or iron fertilization. However, further investigation is required to reconstruct the extent of Southern Ocean frontal migrations before, during, and after the MPT, while also distinguishing other potential complicating factors, such as alterations in deep ocean stratification and water-mass geometry.

1 Introduction

Changes in ice sheets, ocean circulation, and biogeochemical processes during Pleistocene glacial-interglacial (G-IG) cycles offers valuable insights into the responses of Earth's climate system to both external forcing and internal dynamics. Between around 1.2 and 0.7 Ma, the relationship between climate and external forcing underwent a fundamental shift known as the Mid-Pleistocene Transition (MPT). During this period, the periodicity of glacial cycles extended from 41 kyr (1 kyr = 1000 years) in the Early Pleistocene to ~100 kyr cycles in the Late Pleistocene, despite the lack of significant changes in orbital forcing (Herbert, 2023 and references therein). This new regime, often referred to as the '100-kyr world' was characterized by more intense glacial periods, which not only resulted in the growth of larger continental ice sheets but also culminated in more abrupt terminations (Imbrie et al., 1993). The MPT represents a regime shift in the dynamics of major continental ice sheets relative to insolation cycles (Clark & Pollard, 1998). Nonetheless, the exact cause of this shift remains enigmatic, partly due to the limited availability of continuous reconstructions that encompass the MPT, thereby constraining the understanding of underlying processes. Established theories often ascribe this transformation to prolonged global cooling associated with a long-term decline in atmospheric CO_2 levels (Willeit et al., 2019) or tectonic forcing (Raymo et al., 1988; Hönisch et al., 2009). However, as Herbert (2023) has recently asserted, the observed "decline in time-averaged temperature and $\delta^{18}O$, and the increase in the saw-tooth character of glacial cycles are driven almost entirely by the increasing severity of glacial episodes”. The crux of understanding the MPT is therefore centered on understanding the increasing intensity of glacial intervals and a progressively elevated threshold that insolation must surpass to trigger a deglaciation (Tzedakis et al., 2017).

A compelling explanation for increasing intense glacial periods across the MPT is associated with lower glacial atmospheric CO_2 concentrations (Chalk et al., 2017; Dyez et al., 2018; Hönisch et al., 2009). As the primary reservoir within the carbon cycle that can both sequester and subsequently release CO_2 to the atmosphere on these timescales, oceanic processes are commonly invoked as the predominant factor in glacial-interglacial CO_2 dynamics (Broecker, 1982; Sigman & Boyle, 2000). Effective sequestration over climatically relevant timescales depends on the export of carbon into the ocean’s interior, thus isolating it from the surface ocean and atmosphere through various physical and biogeochemical mechanisms. For example, physical processes such as deep ocean stratification and the presence of sea-ice contribute to the isolation of the deep and bottom water masses wherein sinking biological carbon may accumulate over timescales from decades to millennia (Stephens & Keeling, 2000; Toggweiler, 1999).

Conversely, the release of deeply sequestered carbon back into the atmosphere primarily depends on connecting abyssal and deep waters, notably the Circumpolar Deep Water (CDW), with the surface, predominately occurring in the Southern Ocean as a component of the global ocean Meridional Overturning Circulation (MOC) (Marshall & Speer, 2012). The modern MOC can be characterised as two interconnected circulation cells: a mid-depth cell associated with the formation of North Atlantic Deep Water (NADW) in the Subpolar North Atlantic and Nordic Seas, and a deeper overturning cell linked to the formation of Antarctic Bottom Water (AABW) around Antarctica (Talley, 2013). Once deep waters are upwelled to the surface near Antarctica, a fraction of this water is transported northwards into the mid-latitude Southern Ocean, where it is subject to subduction as Subantarctic Mode Water (SAMW) and Antarctic Intermediate Water (AAIW). This process contributes significantly to the ventilation of the low-latitude thermocline and the return flow of upper ocean waters towards the North Atlantic (Bower et al., 2019). The fate of this carbon and nutrient-rich water, during the phases of upwelling and subsequent downwelling in the Southern mid-latitudes, is critical for determining the efficiency of the global biological carbon pump. Exposure to the atmosphere facilitates the outgassing of oceanic CO_2 while the incomplete biological utilization of nitrate and phosphate represents a missed opportunity for Southern Ocean phytoplankton to effectively sequester CO_2 (Marinov et al., 2006; Primeau et al., 2013). During past glacial intervals, the enhancement of primary productivity in the Subantarctic Zone (SAZ; the Southern Ocean region bounded by the Subtropical Front (STF) to the north and the Subantarctic Front (SAF) to the south; Figure 1), likely mitigated this CO_2 ‘leak’ into the atmosphere, potentially stimulated by iron fertilization linked to dust deposition (Martin, 1990; Martinez-Garcia et al., 2014; Weis et al., 2024). Increasing the efficiency of nutrient utilization in the SAZ has been proposed as a pivotal factor contributing to the reduction of glacial CO_2 concentrations across the MPT (Chalk et al., 2017; Martínez-Garcia et al., 2011). However, additional long-term records of biological pump efficiency in the SAZ remain essential to better understand the role that changes in the Southern Ocean carbon cycle played in Pleistocene glacial cycles.

1.1. Southern Ocean carbon isotope gradient

The biological and thermodynamic processes that partition carbon among the atmosphere, upper- and deep-ocean concurrently drive isotopic fractionation of the carbon species involved. This phenomenon is evidenced by the distribution of $^{13}C/^{12}C$ ratios in Dissolved Inorganic Carbon (DIC) of seawater (Figure 1b), reflecting a complex interplay of the biological, physical, and thermodynamic histories associated with each water mass (Charles et al., 1993; Eide et al., 2017; Kroopnick, 1985). The preferential uptake of ^{12}C during photosynthetic processes results in the enrichment of ^{13}C in the surrounding surface ocean (high $\delta^{13}C$, where $\delta^{13}C = ([(^{13}C/^{12}C)_{DIC} / (^{13}C/^{12}C)_{standard}] - 1) \times 1000$). Conversely, the remineralization of organic matter at depth reduces the $\delta^{13}C_{DIC}$ in deeper waters. Consequently, the vertical gradient between shallow and deep ocean $\delta^{13}C_{DIC}$ is enhanced in scenarios characterized by a more efficient biological carbon pump (Morée et al., 2018). During past intervals of lower atmospheric CO_2 levels on both millennial and glacial-interglacial timescales, the $\delta^{13}C_{DIC}$ gradient between the sub-surface and deep Southern Ocean (hereafter referred to as $\Delta\delta^{13}C_{(sub\text{-}deep)}$) increased (Charles et al., 2010; Ziegler et al., 2013).

In 2013, Ziegler *et al*. reconstructed $\Delta\delta^{13}C_{(sub\text{-}deep)}$ over the past 350 ka by measuring the $\delta^{13}C$ gradient between the deep-dwelling planktic foraminifera (*Globorotalia truncatulinoides sinistral;* D'Orbigny, 1839) and epibenthic foraminifera species (*Cibicoides wuellerstorfi;* Schwager, 1866) from sediment core MD02-2588, recovered from the Agulhas Plateau (41°19.90' S, 25°49.7' E, 2907 m water depth) in the SW Indian Ocean. The study revealed that the $\delta^{13}C$ gradient between *G. truncatulinoides* (representing $\delta^{13}C_{DIC}$ in the permanent thermocline; Chiessi et al., 2007; Hu et al., 2020; Ziegler et al., 2013) and *C. wuellerstorfi* (indicative of $\delta^{13}C_{DIC}$ of deep waters; ~3000m in this study) was found to be largest during full glacial conditions. This finding indicates a stronger chemical gradient between subsurface and deep Southern Ocean waters when atmospheric CO_2 was lowest. Moreover, millennial-scale variations in $\Delta\delta^{13}C_{(sub\text{-}deep)}$ in this record closely corresponded with sub-orbital changes in Southern Ocean iron fluxes and atmospheric CO_2 levels, prompting Ziegler *et al.* to propose a causal relationship between dust-borne iron fertilization and the efficiency of the biological pump.

Recently, Starr *et al.* (2025) presented an extension of the Ziegler *et al.* (2013) $\Delta\delta^{13}C_{sub\text{-}deep}$ record across two key interglacial periods: Marine Isotope Stages 11 and 31. Their analysis demonstrated that minima in $\Delta\delta^{13}C_{(sub\text{-}deep)}$ at the Agulhas Plateau were closely aligned with variations in the latitudinal extent of the Antarctic Circumpolar Current (ACC). Specifically, the poleward intensification of the ACC during peak interglacial conditions corresponded with diminished chemocline strength ($\Delta\delta^{13}C_{(sub\text{-}deep)}$ minima), alongside a reduction in Southern Ocean sea ice extent (Kunz-Pirrung et al., 2002; Scherer et al., 2008), alterations in Antarctic iceberg trajectories towards more southerly paths (Starr et al., 2021), and a decrease in the abundance of polar/subpolar foraminifera species within the mid-latitude Southern Ocean

(Becquey et al., 2002; Marcks et al., 2023). Starr et al. (2025) suggest that during these two prolonged warm interglacial phases, a poleward intensification of the Southern Hemisphere Westerlies (SHW) induced a parallel shift in the ACC, thereby enhancing the upwelling of carbon from the deep Southern Ocean, which ultimately drove minima in $\Delta\delta^{13}C_{(sub\text{-}deep)}$ as well as maxima in atmospheric CO_2 levels.

1.2. This study

In this study, we extend the $\Delta\delta^{13}C_{(sub\text{-}deep)}$ records of Ziegler *et al*. (2013) and Starr et al. (2025) throughout the MPT by incorporating a new high-resolution $\delta^{13}C$ record of *G. truncatulinoides* from the International Ocean Discovery Program (IODP) Site U1475 (41°25.6' S, 25°15.6' E, 2669 m water depth). Site U1475 is located in close proximity to MD02-2588 (Figure 1a), with these sites previously amalgamated into a composite stratigraphy (the Agulhas Plateau Composite; AP_{comp}) (Starr et al., 2021; Starr et al., 2025) (See section 2.1). A continuous record of benthic $\delta^{13}C$ for the AP_{comp} was published by Starr *et al*. (2021), allowing us to combine new measurements with those from Ziegler et al. (2013) (0-300 ka) and Starr et al. (2025) (350 – 460 ka Ma and 1.04-1.20 Ma) in order to present a consistent, near-continuous record of $\Delta\delta^{13}C_{(sub\text{-}deep)}$ spanning 0 – 1.55 Ma. This dataset enables an investigation into critical questions concerning the role of Southern Ocean processes in climate evolution throughout the MPT.

For instance, if the efficiency of the biological pump increased in response to heightened dustiness during glacial periods across the MPT (Chalk et al., 2017), we would expect to observe an increase in $\Delta\delta^{13}C_{(sub\text{-}deep)}$ between pre- and post-MPT glacials, closely correlating with SAZ iron fluxes and atmospheric CO_2 levels. Alternatively, if the biological pump efficiency does not serve as the primary driver for the declining glacial CO_2 levels throughout the MPT, we might expect decoupled variations in $\Delta\delta^{13}C_{(sub\text{-}deep)}$, iron fluxes, and atmospheric CO_2 in terms of timing and/or magnitude.

Additionally, the abrupt weakening of the chemocline strength during deglacial transitions, characterized in the paleoceanographic record by rapid declines in $\Delta\delta^{13}C_{(sub\text{-}deep)}$, has been shown to coincide with deglacial rises in atmospheric CO_2 during the Late Pleistocene (Spero & Lea, 2002). Whether this is driven by the upwelling of $\delta^{13}C$-depleted deep waters (Hu et al., 2020; Ninnemann & Charles, 1997; Spero & Lea, 2002) or due to air-sea exchange effects (Lynch-Stieglitz, 2019; Shao et al., 2021), these shallow and intermediate $\delta^{13}C$ minima (termed Carbon Isotope Minima Events; CIMEs) appear to be a consistent signature of post-MPT terminations. Our new record affords the opportunity to explore whether CIMEs and rapid breakdown in chemocline strength represent distinctive characteristics of post-MPT deglaciations.

2 Materials and Methods

2.1. Core Site

The Agulhas Plateau composite (AP_{comp}) constitutes a stratigraphic framework that incorporates proximal sediment core sites MD02-2588 and International Ocean Discovery Program Site

U1475 (Figure 1). These sites are situated in the northernmost SAZ, close to the present-day location of the STF, which is recognised as a significant biogeochemical boundary delineating the colder, nutrient-rich waters of the SO from the warmer, saline and nutrient-poor surface waters of the Agulhas Current. The latter subsequently returns to the subtropical Indian Ocean via the Agulhas return current (Lutjeharms, 2006). We employ the "LR04" age model (Lisiecki & Raymo, 2005) constructed for the AP_{comp} by Starr *et al*. (2021), aligning the benthic $\delta^{18}O$ record with an updated global $\delta^{18}O$ benthic stack (Ahn et al., 2017) in addition to 12 previously published radiocarbon dates (Ziegler et al., 2013). Our sample selection follows Starr *et al*. (2021), and we make use of previously published records of $\delta^{13}C$ and $\delta^{18}O$ from *G. truncatulinoides* and *C. wuellerstorfi* from MD02-2588 (0 – 300 ka; n = 783; Ziegler et al., 2013) and Site U1475 (0.35 - 0.46 Ma and 1.04-1.2 Ma; n = 237; Starr et al., 2025) as well as *C. wuellerstorfi* from Site U1475 (0.30 – 1.55 Ma; Starr et al., 2021). Although co-registered samples were obtained at the same resolution as described in Starr et al. (2025) the scarcity of *G. truncatulinoides* specimens constrains the resolution of the resultant isotope record during some intervals.

2.2. Stable isotope measurements

Down-core stable isotope records ($\delta^{18}O$, $\delta^{13}C$) were obtained for sinistral (left-coiling) *G. truncatulinoides* (hereafter *G. truncatulinoides* refers to the sinistral form unless otherwise stated) specimens from the 250-315 µm size fraction. The number of specimens measured in each sample ranged from 3 to 15. Isotope analyses of large samples ($n>7$) were measured using a Finnigan Delta V Advantage coupled online with a Gasbench II, and smaller samples ($n\leq7$) were measured using a Thermo Finnigan MAT 253 mass spectrometer coupled online to a Carbo Kiel carbonate preparation device at Cardiff University. All results are calibrated to an internal laboratory standard (BCT63; $\delta^{18}O$ = -1.93‰; $\delta^{13}C$ = 2.07‰) and reported relative to the Vienna Pee Dee Belemnite scale. The long-term precision of the internal laboratory standard was better than ±0.05‰ for $\delta^{18}O$ and ±0.025‰ for $\delta^{13}C$ (±1σ) for MAT 253 measurements and ±0.06 for $\delta^{18}O$ and ±0.05 for $\delta^{13}C$ for Delta V measurements.

Measurements of *C. wuellerstorfi* $\delta^{18}O$, $\delta^{13}C$ are taken from Starr et al. (2021), who measured 2-3 well preserved specimens in the 250–315 µm size fraction following the same methodology as the "small sample" *G. truncatulinoides* protocol described above. The *C. wuellerstorfi* measurements by Starr et al. (2021) were made on the same Thermo Finnigan MAT 253 used in this study, with the same internal calibration and long-term precision. Stable isotope gradients between *G. truncatulinoides* and *C. wuellerstorfi* ($\Delta\delta^{13}C_{(sub\text{-}deep)}$) were obtained from co-occurring measurements of each species within the same stratigraphic samples, where $\Delta\delta^{13}C_{(sub\text{-}deep)} = \delta^{13}C_{G.\ truncatulinoides} - \delta^{13}C_{C.\ wuellerstorfi.}$

2.3. Assessing Uncertainty with Individual Foraminifera Analysis

Planktic foraminifera species typically exhibit greater inter-test variability compared to benthic species within a specific stratigraphic sample. This can be attributed to the heightened seasonal, inter-annual, and decadal climate variations in the upper ocean relative to deeper waters. Consequently, a larger number of planktic shells are generally necessary per sample to yield a representative estimate of the population mean (Fraass & Lowery, 2017). To constrain the relationship between precision and the number of shells in this study, $\delta^{18}O$ and $\delta^{13}C$ were measured on 154 individual *G. truncatulinoides* shells spanning 4 samples from Site U1475 (Figure S1), following the small sample protocol described above. The resulting standard deviations (averaged across the 4 samples after the subtraction of the sample means) divided by the square root of the number of shells measured (*n*) provide the standard error of the mean (Figure 2). For *n = 1*, the resulting standard errors were 0.40‰ and 0.30‰ for $\delta^{18}O$ and $\delta^{13}C$, respectively. For a sample comprising *n = 15* specimens, the standard error obtained was 0.08‰ for $\delta^{18}O$ and 0.06‰ for $\delta^{13}C$ (Figure 2c). In our downcore isotope records, datapoints consisting of *n <= 3* specimens (with standard error for *n = 3* recorded at 0.23‰ for $\delta^{18}O$ and 0.18‰ for $\delta^{13}C$) were excluded, as this threshold represents the minimal number of specimens below which analytical error exceeds the inter-sample standard deviation. The corresponding error of the remaining downcore data points is reported to ensure transparency where the number of available *G. truncatulinoides* specimens varied. A record of the number of specimens measured per sample for the MD02-2588 dataset is unavailable. Nonetheless, Ziegler et al. (2013) indicate that "~10 individuals" were selected per sample. Thus, we adopt *n = 10* to attribute analytical uncertainty to these data (i.e. the upper ~300 ka of the spliced AP_{comp} isotope records presented herein).

2.4. Marine Isotope Stage Analysis

To ascertain a representative value for each Marine Isotope Stage (MIS), data were first binned (bin size of 2.5 kyr) to standardize the variable resolution effects both within a particular record and across different records. The errors associated with the binned data are expressed as one standard error of the mean (1 SE) derived from the standard deviation of the input data points divided by the square root of their number. In instances where analytical uncertainties were available, these were incorporated into the binning error during the propagation process. Two criteria were employed to designate each binned data point as either 'glacial' or 'interglacial'. First, each data point was assigned an MIS label according to the age model and the LR04 MIS boundaries from Lisiecki and Raymo (2005). Second, a label of 'glacial' or 'interglacial' was assigned based on the value of the corresponding data point on a detrended $\delta^{18}O_{benthic}$ record, with values <0 categorized as 'interglacial' and those ≥0 as 'glacial'. This methodology refines the LR04 MIS boundaries and accommodates potential discrepancies between the employed model and the LR04.

Following the assignment of MIS labels, any MIS for which a record had <3 binned data points was excluded to minimize the influence of sampling gaps or outliers (for example, several MISs were omitted from the atmospheric CO_2 proxy record due to the discontinuous availability of CO_2 reconstructions prior to 800 ka). Subsequently, we evaluated two methodologies to ascertain the representative proxy value for each remaining MIS. The first approach involved calculating the mean value for each stage, propagating both the analytical and binning uncertainties through 10000 iterations of bootstrap and Gaussian sampling. This method proposes that the average value within a glacial or interglacial period effectively represents that given interval. While the mean value approach minimizes the influence of outliers and does not necessitate *a priori* assumptions of the sign of glacial-interglacial variability, it may underestimate the true magnitude of this variability by incorporating ‘intermediate’ data points not associated with peak glacial/interglacial conditions (Tzedakis et al., 2009). The second method sought to identify bootstrap maximum and minimum values (again employing 10000 iterations of Gaussian sampling for uncertainty estimation) within each stage, with the maximum or minimum value assigned based on existing *a priori* knowledge regarding whether the given proxy has maxima or minima during glacial stages. Notably, this approach carries the risk of artificially amplifying weak or absent glacial-interglacial variability (e.g., by taking the maximum value for a glacial and minimum for an interglacial). However, we contend that this second approach yields a more informative representation of MIS intensity. It is worth noting that due to the “double filtering” applied in assigning glacial or interglacial labels, some stages (for example, MIS 23) are entirely excluded from the final table. This is because, despite the LR04 MIS being classified as odd-numbered, the detrended $\delta^{18}O_{benthic}$ consistently remains above 0, thereby precluding the stage from being classified as sufficiently “interglacial”.

3 Results and Discussion

3.1. $\delta^{13}C$ results

The $\delta^{13}C$ of *G. truncatulinoides* ($\delta^{13}C_{trunc}$) and *C. wuellerstorfi* ($\delta^{13}C_{cib}$) at the Agulhas Plateau are broadly characterized by glacial-interglacial variability, with maxima (minima) occurring during interglacial (glacial) intervals (Figure 3). While marked glacial-interglacial variations dominate the benthic $\delta^{13}C$ record (Figure 3), G-IG variations in $\delta^{13}C_{trunc}$ are more muted compared to lower-frequency variability. These long-term fluctuations in $\delta^{13}C_{trunc}$ are similar to those previously documented in low latitude planktic $\delta^{13}C$ records, such as the $\delta^{13}C$ stack of *Globigerinoides ruber* from the Mediterranean (Wang et al., 2010) and the *Globigerinoides sacculifer* $\delta^{13}C$ record from Ocean Drilling Program (ODP) Site 806 in the western equatorial Pacific (Berger et al., 1993) (Figure S2). Both these planktic $\delta^{13}C$ records are marked by intervals of sustained elevated $\delta^{13}C$, relative to their corresponding benthic $\delta^{13}C$ records, between MIS 8 and MIS 12 as well as between MIS 16 and MIS 24. These extended cycles are intermittently punctuated by $\delta^{13}C_{trunc}$ minima in AP_{comp} that coincide with most glacial terminations, and where values converge with $\delta^{13}C$ benthic (e.g. 0.86 Ma). Such excursions are recognizable as the carbon isotope minima events (CIMEs) that have been identified in records of surface and (well-ventilated) intermediate water masses in the Atlantic, Indian and Pacific Oceans (Figure S2; Hu et al., 2020; Oppo & Fairbanks, 1989; Romahn et al., 2014; Spero & Lea, 2002; Ziegler et al., 2013; Bolton et al., 2013; Nascimento et al., 2021, Scussolini and Peeters, 2013).

Ziegler et al. (2013) indicate that *G. truncatulinoides* inhabit the deep thermocline in the Agulhas Plateau region. This conclusion is corroborated by core-top measurements of $\delta^{18}O_{trunc}$ and $\delta^{13}C_{trunc,}$ which suggest potential calcification depths ranging from 300 to 400m. These findings are consistent with plankton tow studies that widely document *G. truncatulinoides* occurring below the fluorescence maxima and pycnocline depths in both the Southern Ocean (Mortyn and Charles, 2002) and the eastern South Atlantic (Lessa et al., 2020). This depth habitat range situates *G. truncatulinoides* distinctly within the recognized distribution of SAMW across the subtropical South Atlantic, subtropical South Indian, and Subantarctic Southern Ocean (Feucher et al., 2019), although we note that the range and composition of SAMW may have varied on the timescales considered in this study.

The discontinuous occurrence of morphologically distinct *G. truncatulinoides* specimens in certain sections of Site U1475 resulted in gaps in the isotope time series, such as between MIS 25 – 26, MIS 40 – 41, and MIS 44 – 46. Although a quantitative record of *G. truncatulinoides* abundance is lacking, the absence of specimens during these intervals might be indicative of adverse environmental or ecological pressures. Within the morphologically defined *G. truncatulinoides* species, five cryptic genotypes have been identified in modern populations (Quillévéré et al., 2013), displaying distinct hydrographic tolerances and consequently, varied geographic distributions. The emergence and adaptation of these genotypes might account for temporal changes in the oceanographic range of *G. truncatulinoides* with the fossil record (Sexton & Norris, 2008). However, it is noteworthy that no divergence events appear to align with the observed low abundance intervals at AP_{comp}. Indeed, the dispersal of *G. truncatulinoides* to its present geographic distribution was completed by ~2 Ma (Sexton & Norris, 2008).

Finally, previous studies have critically evaluated the applicability of benthic $\delta^{13}C$ records in documenting extensive changes in water mass distribution and ocean circulation changes during the Pleistocene (Hodell et al., 2003; Hines et al., 2024). The AP_{comp} $\delta^{13}C_{cib}$ record exhibits a close correlation with G-IG cycles and longer-term fluctuations observed in proximal sites, such as Site U1479 (35°S, 14°E, 2615m water depth; Hines et al., 2024) and ODP Site 1090 (43°S, 9°E, 3702m water depth; Hodell et al., 2003). This is demonstrated in Hines et al. (2024), who show that variations in the proportion of "Northern-Sourced Waters" (i.e. deep waters originating from the North Atlantic) at Site U1479, as determined using quasi-conservative authigenic Neodymium records, can account for a significant portion of the observed signal in benthic $\delta^{13}C_{cib}$. They also report no signs of a significant shift in deep ocean circulation during the MPT. Likewise, Starr et al. (2021) also demonstrate that a binary water-mass mixing model incorporating Pacific Deep Water and northern North Atlantic end members exhibits a strong correlation with the AP_{comp} $\delta^{13}C_{cib}$ ($r = 0.75$).

3.2. Carbon isotope gradient

Both $\delta^{13}C_{trunc}$ and $\delta^{13}C_{benthic}$ exhibit the imprint of large-scale secular changes within the whole-ocean $\delta^{13}C$ pool (Hoogakker et al., 2006). However, this signal is theoretically cancelled out in $\Delta\delta^{13}C_{(sub-deep)}$. Glacial-interglacial variations in $\Delta\delta^{13}C_{(sub-deep)}$ are markedly more pronounced than in either constituent record, with stronger gradients correlated with glacial periods and weaker gradients associated with terminations and interglacials (Figures 3 and 4). Glacial $\Delta\delta^{13}C_{(sub-deep)}$ maxima range from ~1 ‰ to ~1.5‰, while interglacial minima span from ~0.5‰ to ~0.0‰, with long-term fluctuations modulating the amplitudes of both. Glacial $\Delta\delta^{13}C_{(sub-deep)}$ values can be broadly grouped into three intervals. The first interval, from MIS 54 to MIS 31 (1.58 – 1.06 Ma; hereafter termed interval I or 'pre-MPT' interval) has an average glacial

$\Delta\delta^{13}C_{(sub\text{-}deep)}$ of 0.68 ± 0.02‰ (calculated as the average value of all samples classified as glacial according to the criteria described above). The average glacial intensity (following the maximum intensity MIS approach described above) in interval I is 1.05‰, with the most intense glacial being MIS 38 (1.25 ± 0.14‰) and the least intense being MIS 48 (0.87 ± 0.10‰) (Figure 5). The second interval exists between MIS 30 and MIS 10 (1.06 – 0.37 Ma; hereafter termed interval II), within which the average glacial $\Delta\delta^{13}C_{(sub\text{-}deep)}$ value is 0.86‰ ± 0.01‰ and the average glacial intensity is 1.29‰ ± 0.15‰. The most intense glacials with respect to $\Delta\delta^{13}C_{(sub\text{-}deep)}$ in this interval are MIS 18 (1.42 ± 0.06‰) and MIS 30 (1.44 ± 0.17‰), while the weakest is MIS 24 (1.13 ± 0.12‰). The final interval, spanning MIS 9 to MIS 1 (the last 0.37 Ma; hereafter termed interval III or 'Late Pleistocene' interval), exhibits an average glacial value of 0.70 ± 0.01‰ and an average glacial intensity of 0.95‰. Within interval III (the Late Pleistocene post-MIS 10), the most intense glacial is MIS 6 (1.08 ± 0.03‰), and the weakest is MIS 2 (0.84 ± 0.03‰). Table 1 presents the average sample values for glacials across each interval.

Interglacial $\Delta\delta^{13}C_{(sub\text{-}deep)}$ follows a comparable long-term trend to glacials, with average interglacial values during interval II being 0.58 ± 0.01‰, in contrast to 0.41 ± 0.01‰ for interglacials in interval I and 0.38 ± 0.01‰ in interval III. The most intense interglacials with respect to $\Delta\delta^{13}C_{(sub\text{-}deep)}$ (following the maximum intensity approach) are MIS 5 (-0.01 ± 0.03‰) and MIS 31 (-0.01 ± 0.06‰), while the least intense interglacials are MIS 27 (0.64 ± 0.09‰), MIS 21 (0.44 ± 0.10‰) and MIS 23 (0.42 ± 0.19‰).

Carbon isotope minima events detected in the $\delta^{13}C_{trunc}$ record manifest in the $\Delta\delta^{13}C_{(sub\text{-}deep)}$ record as breakdowns in chemocline strength, wherein $\Delta\delta^{13}C_{(sub\text{-}deep)}$ values approach 0‰. Besides the CIMEs identified by Ziegler *et al*. (2013) at the terminations of MIS 2, 6, and 8, additional breakdowns are noted during several terminations extending back to the transition from MIS 52 to 51 (ca. 1.52 Ma) (Figure 4). However, while $\Delta\delta^{13}C_{(sub\text{-}deep)}$ consistently decreases by at least ~0.5‰ between glacial and interglacial stages, not all terminations are marked by a complete gradient collapse (values nearing ~0‰). For example, Terminations TIV, TVI, TVIIa, TVIII, TIX, and TXVII demonstrate relatively muted and/or gradual in nature shifts (Figure 4). We note that variations in sedimentation, sampling rate, and inherent chronological uncertainties preclude us from defining a quantity (rate/magnitude) marking chemocline collapse.

In the simplest terms, $\Delta\delta^{13}C_{(sub\text{-}deep)}$ indicates how similar the carbon isotope composition of calcite precipitated by *G. truncatulinoides* (in SAMW) and by *C. wuellerstorfi* (in some mix of CDW and NADW) is. Consequently, variations in the preformed $\delta^{13}C$ of SAMW and/or CDW and NADW, potentially influenced by factors such as seawater temperature, the rate of air-sea exchange, changes in water mass mixing, and ocean circulation, can complicate the interpretation of $\Delta\delta^{13}C_{(sub\text{-}deep)}$ as a proxy for biological pump efficiency. We review these factors below before exploring the implications of the $\Delta\delta^{13}C_{(sub\text{-}deep)}$ proxy records.

3.3. Drivers of $\Delta\delta^{13}C_{(sub\text{-}deep)}$

In the modern ocean, temperature-dependent fractionation during air-sea CO_2 exchange results in SAMW being relatively enriched in $\delta^{13}C$ compared to global nutrient stoichiometry (Charles et al., 1993; Eide et al., 2017). Consequently, $\Delta\delta^{13}C_{(sub\text{-}deep)}$ can be sensitive to changes in the preformed $\delta^{13}C$ of SAMW linked to the temperature and/or the rate of air-sea exchange in the SAZ. Air-sea exchange at lower (higher) temperatures leads to a more enriched (depleted) $\delta^{13}C$ of SAMW, which in turn affects $\Delta\delta^{13}C_{(sub\text{-}deep)}$ (independent of biological export) (Mook et al., 1974). To explore the potential thermodynamic effects on the evolution of $\Delta\delta^{13}C_{(sub\text{-}deep)}$ throughout the MPT, we employ two approaches. First, we evaluate whether changes in SAZ Sea Surface Temperature (SST) can account for the long-term fluctuations in $\Delta\delta^{13}C_{(sub\text{-}deep)}$ through temperature-dependent air-sea fractionation. We utilize the alkenone SST record from ODP Site 1090 (Martínez-Garcia et al., 2009; 2011), located in the Atlantic SAZ, where much of the SAMW bathing the AP_{comp} would have most recently been in contact with the atmosphere (Sallée et al., 2010). All else being equal, a warming of 2ºC would be necessary to account for the ~0.2‰ decrease in $\Delta\delta^{13}C_{(sub\text{-}deep)}$ between Interval II and Interval III (assuming a 0.1‰ enrichment per 1ºC of cooling; (Mook et al., 1974)). However, the ODP 1090 alkenone SST record shows no statistically significant warming during glacials across the two intervals (Figure S3). This is consistent with observations of relatively stable Southern Ocean SSTs during glacials over the past ~0.80 Ma (Becquey & Gersonde, 2002; Clark et al., 2024; Ho et al., 2012). Furthermore, while SST reconstructions indicate a cooling in the Southern Ocean at the onset of the MPT, the timing of this cooling precedes the observed increase in $\Delta\delta^{13}C_{(sub\text{-}deep)}$ between Intervals I and II. Notably, the coldest glacial in the ODP 1090 SST record is MIS 34, which corresponds to a relatively weak $\Delta\delta^{13}C_{(sub\text{-}deep)}$ (1.09‰).

Secondly, we follow Ziegler *et al*. (2013) in inferring temperature changes from the stable oxygen isotope gradient between *G. truncatulinoides* and *C. wuellerstorfi* at the AP_{comp} ($\Delta\delta^{18}O_{(sub\text{-}deep)}$). In this context, global ice volume effects are cancelled out in the $\Delta\delta^{18}O_{(sub\text{-}deep)}$ record, and given that variations in benthic temperature are likely minimal (since the deep water at 3000m is already near-freezing), the changes in the ice-volume corrected $\delta^{18}O$ of *G. truncatulinoides* emerge as the key factor driving $\Delta\delta^{18}O_{(sub\text{-}deep)}$ fluctuations (Ziegler et al., 2013). Acknowledging several caveats, we derive a first-order estimate of the SAMW temperature change from $\Delta\delta^{18}O_{(sub\text{-}deep)}$. Specifically, the 2ºC warming of SAMW necessary to account for the 0.2‰ decrease in $\Delta\delta^{13}C_{(sub\text{-}deep)}$ between Intervals II and III should generate a more pronounced temperature gradient between SAMW and the deep water, thereby producing an intensified $\Delta\delta^{18}O_{(sub\text{-}deep)}$ gradient. This would imply a greater disparity in $\delta^{18}O$ between *G. truncatulinoides* and *C. wuellerstorfi* $\delta^{18}O$, indicating a more negative $\Delta\delta^{18}O_{(sub\text{-}deep)}$ gradient. Instead, the $\Delta\delta^{18}O_{(sub\text{-}deep)}$ record reveals a long-term trend towards less negative values. This trend is comparable in sign and magnitude (using the approximate sensitivity of 0.25‰ per 1ºC for $\Delta\delta^{18}O$ (Kim & O'Neil, 1997)) to the 1.2 ºC per Ma cooling trend reconstructed for intermediate water in the SW Pacific (McClymont et al., 2016). Consequently, instead of warming, which would lead to a more negative $\Delta\delta^{18}O_{(sub\text{-}deep)}$ gradient, the data show a statistically significant shift to less negative $\Delta\delta^{18}O_{(sub\text{-}deep)}$ values, indicative of SAMW cooling between the two intervals (*t-test statistic = 7.15, p =* $<1x10^{10}$).

This analysis indicates that temperature-dependent fractionation during air-sea CO_2 exchange in SAMW source waters is unlikely to explain the long-term fluctuations observed in $\Delta\delta^{13}C_{(sub\text{-}deep)}$. However, non-biological factors such as variations in the rate of air-sea exchange, potentially influenced by wind speed or sea ice cover, could also cause shifts in $\Delta\delta^{13}C_{(sub\text{-}deep)}$.

These effects, along with the diverse responses of associated water masses, introduce uncertainties when interpreting individual foraminifera records from a single site. For example, Lear et al. (2016) suggested that changes in benthic $\delta^{13}C$ across the MPT in the deep North Atlantic reflect a significant air-sea exchange signal driven by changes in sea-ice cover in deep water formation regions. If correct, this would decouple deep $\delta^{13}C$ (and thus, $\Delta\delta^{13}C_{(sub\text{-}deep)}$) from the broader increase in deep ocean carbon storage, which is thought to have occurred across the MPT (Farmer et al., 2019).

To more quantitatively explore the potential sensitivity of $\Delta\delta^{13}C_{(sub\text{-}deep)}$ to biological and non-biological influences, we investigate changes in $\Delta\delta^{13}C_{(sub\text{-}deep)}$ based on the carbon isotope sensitivity experiments conducted by Morée *et al*. (2018) using an ocean biogeochemistry general circulation model (HAMOCC2s). These experiments varied parameters such as sea ice extent, gas exchange rate, organic carbon export, and nutrient utilization efficiency in the Southern Ocean, focusing on their impacts on vertical carbon isotope gradients. The most notable responses in the vertical carbon isotope gradient between model cells representing the subsurface and deep water at the AP_{comp} site (i.e., the model realization of our $\Delta\delta^{13}C_{(sub\text{-}deep)}$) were observed with increased SAZ nutrient uptake efficiency (analogous to Fe fertilization) and higher particulate carbon sinking rates, both of which raise $\Delta\delta^{13}C_{(sub\text{-}deep)}$ (Figure S4). Conversely, less efficient particulate organic carbon export and an increase in Southern Ocean sea-ice extent leads to a decrease in $\Delta\delta^{13}C_{(sub\text{-}deep)}$, primarily due to reduced productivity resulting from the expanded sea ice rather than limitations on air-sea exchange (Morée et al., 2018). Additionally, changes in the rate of air-sea exchange in the Southern Ocean have only a minor influence on $\Delta\delta^{13}C_{(sub\text{-}deep)}$. This may be attributed to the prolonged equilibration time of $\delta^{13}C$, which hinders the impact of air-sea exchange on $\delta^{13}C$, allowing biological processes to dominate the $\delta^{13}C$ and consequently $\Delta\delta^{13}C$ (Eide et al., 2017; Morée et al., 2018; Murnane & Sarmiento, 2000). Furthermore, it is also worth noting that a change in the rate of air-sea exchange in the Southern Ocean, for example, due to surface stratification or sea-ice cover, would likely also drive alterations in atmospheric CO_2 by affecting outgassing (Stephens & Keeling, 2000) and deep-water stratification around Antarctica (Ferrari et al., 2014).

3.4. Glacial $\Delta\delta^{13}C_{(sub\text{-}deep)}$ *across the MPT*

Considering the complexities in interpreting our $\Delta\delta^{13}C_{(sub\text{-}deep)}$ record, we now revisit the two hypotheses previously introduced in this paper. Firstly, we consider the relationship between biological pump efficiency, $\Delta\delta^{13}C_{(sub\text{-}deep)}$, and atmospheric CO_2 levels during the MPT. Chalk *et al*. (2017) propose that glacial CO_2 concentrations decreased from the pre-MPT (>MIS 30) to post-MPT (<MIS 8 in their study), attributing this change to an increase in dust-borne iron fertilization of the Southern Ocean. Conversely, Farmer et al. (2019) argue that the timing of the rise in glacial Fe flux during the MPT does not align with the expected timing of atmospheric CO_2 decrease, as the former occurs too early in the MPT. In the modern Southern Ocean, iron acts as a limiting nutrient in phytoplankton growth (Martin, 1990). Thus, an increase in iron

availability (such as from wind-blown dust) during glacial periods may enhance the efficiency of nutrient utilization processes. Ziegler *et al*. (2013) documented that maxima in $\Delta\delta^{13}C_{(sub\text{-}deep)}$ over the past 350 ka align with peaks in dust deposition observed in the South Atlantic and Antarctic ice cores, consistent across both orbital and sub-orbital timescales. Moreover, geochemical investigations indicate that dust-borne iron supplied to the Southern Ocean during Late Pleistocene glacial periods was likely bioavailable (Shoenfelt et al., 2018) and effectively enhanced nutrient utilization (Martínez-García et al., 2014) and export productivity (Anderson et al., 2014) in the SAZ. Although robust evidence supports the link between dust fertilization and productivity in the Southern Ocean during Late Pleistocene glacials and modeling studies suggest that this mechanism alone might account for 20-40 ppm of the total CO_2 reduction seen during the Last Glacial Maximum (Hain et al., 2010; Lambert et al., 2015), questions remain on how this mechanism evolved or contributed during the MPT. A key outstanding question here is whether the observed decrease in glacial CO_2 levels scale to the magnitude of dust-borne iron fertilization during the MPT.

Our new $\Delta\delta^{13}C_{(sub\text{-}deep)}$ record presents a valuable opportunity to examine the relationship between the strength of the glacial chemocline during the MPT and variations in Southern Ocean iron supply and atmospheric CO_2 levels. For example, if we posit that the $\Delta\delta^{13}C_{(sub\text{-}deep)}$ record is primarily influenced by biological export in the SAZ and that the Southern Ocean biological pump is a key driver of the atmospheric CO_2 decline across the MPT, we would anticipate the strength of the glacial chemocline at the AP_{comp} to scale with the magnitude of Fe accumulation in the SAZ and atmospheric CO_2 levels across different glacial periods. The long-term trend of increasing mean global $\delta^{18}O$ throughout the earlier Plio-Pleistocene (Lisiecki & Raymo, 2005), which reflects the expansion of continental ice sheets and cooling of the deep ocean since ~2.8 Ma, is echoed in the rising glacial Fe accumulation at ODP Site 1090 in the Atlantic SAZ (Martínez-Garcia et al., 2011). Additionally, a stepwise increase in glacial Fe accumulation and a concurrent decrease in glacial CO_2 levels are observed across the MPT; however, pinpointing the timing of each change-point remains challenging due to the limitations of existing records (Figure S5), which complicates the establishment of a definitive causal relationship (Farmer et al., 2019). As detailed in Table 1, mean glacial $\Delta\delta^{13}C_{(sub\text{-}deep)}$ values increase between the pre-MPT (interval I) and the MIS 30-10 interval (interval II). A two-sided *t-test* comparing $\Delta\delta^{13}C_{(sub\text{-}deep)}$ from glacial samples in these two intervals confirms that this increase is statistically significant ($t = 4.4, p < 1x10^{-4}$). On face value, these findings seem to corroborate the hypothesis of a more efficient biological pump operating in concert with lower glacial CO_2 levels across the MPT.

Biomarker accumulation records from the Agulhas Plateau (Cartagena-Sierra et al., 2021; Tangunan et al., 2021) reveal broadly opposing long-term trends to AP_{comp} $\Delta\delta^{13}C_{(sub\text{-}deep)}$. Specifically, glacial alkenone accumulation reaches its lowest levels between MIS 22 to MIS 12, coincident with the highest glacial $\Delta\delta^{13}C_{(sub\text{-}deep)}$. While no singular measure of productivity, such as biomarker, organic carbon, or opal accumulation, fully accounts for the long-term variations observed in glacial $\Delta\delta^{13}C_{(sub\text{-}deep),}$ it is plausible to suggest that $\Delta\delta^{13}C_{(sub\text{-}deep)}$ reflects an integrated signal representing a larger area of Southern Ocean export productivity than is captured by productivity records at a single site.

The comparison shown in Figure 6 between glacial intensity among the MISs represented by intervals I and II reveals a strong correlation between $\Delta\delta^{13}C_{(sub\text{-}deep)}$ and SAZ Fe accumulation ($r = 0.67$, $p<0.005$), as well as between $\Delta\delta^{13}C_{(sub\text{-}deep)}$ maxima and CO_2 minima ($r = -0.76$, $p<0.005$). This suggests that glacial intervals characterised by a more pronounced chemocline were associated with higher SAZ Fe fluxes and lower CO2 levels prior to the Late Pleistocene. This observation further implies that glacial intensification during the MPT was linked to increased iron fertilization in the SAZ, likely as a response to gradual cooling and heightened aridity in the Southern Hemisphere (Clark et al., 2024). Despite the apparent importance of Fe fertilization, the stronger correlation between CO_2 and $\Delta\delta^{13}C_{(sub\text{-}deep)}$ relative to the correlation between SAZ Fe and $\Delta\delta^{13}C_{(sub\text{-}deep)}$ (as assessd by Pearson's correlation coefficient r) nonetheless implies a closer relationship between SO chemocline strength and atmospheric CO_2 levels than Fe fluxes and atmospheric CO_2. It is important to be cautious in distinguishing correlation from causation, which underscore the necessity of considering additional processes to explain the entire variations in interglacial-glacial CO_2 levels (Hain et al., 2010). Around ~1.50 Ma, a decline in Southern Hemisphere extratropical SST resulted in an expansion of Southern Ocean sea-ice (An et al., 2024; Clark et al., 2024; Starr et al., 2021), subsequently enhancing the formation of bottom waters around Antarctica, increasing deep ocean stratification and carbon storage (Farmer et al., 2019), while also contributing to cooling in the Northern Hemisphere (An et al., 2024). Furthermore, a stepwise increase in the northern reach of Antarctic iceberg melting around ~1.25 Ma (again, potentially in response to the observed declines in SST) would have driven further stratification and strengthened the Southern Ocean chemocline (Hasenfratz et al., 2019; Starr et al., 2021). These processes, influencing carbon partitioning in the ocean's interior, may result in changes in $\Delta\delta^{13}C_{(sub\text{-}deep)}$ and CO_2, though they do not directly affect iron fluxes. Nevertheless, potential feedback mechanisms involving CO_2, global cooling, and continental dust emissions could complicate this interpretation (Willeit et al., 2019). Furthermore, temporal changes in the bioavailability of iron, for example, possibly due to variations in the provenance of dust or iceberg-rafted sediment, could also lead to a decoupling of iron fluxes from the efficiency of the biological pump.

3.5. Chemocline – CO_2 decoupling in the Late Pleistocene

The strength of the SO chemocline appears to have diminished after MIS 10, evidenced by glacial $\Delta\delta^{13}C_{(sub\text{-}deep)}$ values reverting to pre-MPT levels. Notably, the $\Delta\delta^{13}C_{(sub\text{-}deep)}$ data derived from glacials in Interval I and Interval III are statistically indistinguishable ($t = 0.52$, $p > 0.5$). In contrast, the return to pre-MPT levels does not extend to atmospheric CO_2 or SAZ iron fluxes, which are statistically indistinguishable between Interval II and Interval III (Figure S5; Table 1). The apparent decoupling between glacial $\Delta\delta^{13}C_{(sub\text{-}deep)}$, SAZ Fe fluxes, and CO_2 levels post-MIS 10 implies that either non-biological pump factors are influencing $\Delta\delta^{13}C_{(sub\text{-}deep)}$ (as outlined in

Section 4.1) or that the strength of the Southern Ocean chemocline is not the pivotal factor governing glacial CO_2 levels during this Late Pleistocene period.

One factor to consider is whether the full magnitude of the $\Delta\delta^{13}C_{(sub\text{-}deep)}$ is consistently recorded at our site over time, given that previous studies suggest the polar region may have expanded during the intensification of late Pleistocene glaciations (Gray et al., 2023; Kohfeld et al., 2013). In the case of non-stationarity, a shift in the position of the Southern Ocean fronts and associated isotope gradients relative to the AP_{comp} site may drive a disconnect between the $\Delta\delta^{13}C_{(sub\text{-}deep)}$ at the AP_{comp} site and atmospheric CO_2 during late Pleistocene glaciations. The distribution of Suess-corrected $\delta^{13}C_{DIC}$ (Eide et al., 2017) in the modern SAZ between 20º and 30ºE (Figure 7), shows that $\Delta\delta^{13}C_{(sub\text{-}deep)}$ would be higher if the AP_{comp} were located both slightly north or slightly south of its current position. In other words, if the STF migrated poleward from its current location, *G. truncatulinoides* at the AP_{comp} site would calcify in more enriched $\delta^{13}C_{DIC}$ subtropical waters (driving higher $\Delta\delta^{13}C_{(sub\text{-}deep)}$). Conversely, should the SAZ expand equatorward from its present position, *G. truncatulinoides* at the AP_{comp} would calcify in more subantarctic water, leading again to a higher $\delta^{13}C$ DIC and thus $\Delta\delta^{13}C_{(sub\text{-}deep)}$ (Eide et al., 2017). Thus, the observed reduction in $\Delta\delta^{13}C_{(sub\text{-}deep)}$ between the Middle to Late Pleistocene could be attributed to *either* a poleward contraction *or* an equatorward expansion of the SAZ (imagine moving the red marker in Figure 7 towards its current position from either the right or left). In other words, $\Delta\delta^{13}C_{(sub\text{-}deep)}$ cannot alone tell us whether frontal locations shifted poleward or equatorward. However, if we also consider $\Delta\delta^{18}O_{(sub\text{-}deep)}$ at the AP_{comp} (see Figure 7b and c), it is clear that only expansion of the SAZ (i.e. more subantarctic waters at the AP_{comp} site) could account for the decrease in both $\Delta\delta^{13}C_{(sub\text{-}deep)}$ and $\Delta\delta^{18}O_{(sub\text{-}deep)}$ between the Middle and Late Pleistocene (intervals II and III). The inset in Figure 7a illustrates a plausible trajectory of glacial averages across the three intervals (I, II, and III; as defined in Table 1) in $\Delta\delta^{13}C_{(sub\text{-}deep)}$ versus $\Delta\delta^{18}O_{(sub\text{-}deep)}$ space.

While contemporary seawater isotope data is not a direct analog for the glacial $\delta^{13}C_{DIC}$ and predicted $\delta^{18}O$ of calcite, this comparison offers some insight into the potential signatures of an expansion of the SAZ in relation to the location of AP_{comp}. Notably, such an expansion of the Southern Ocean between the Middle and Late Pleistocene would itself potentially facilitate a reduction in glacial CO_2 levels through its influence on wind patterns and upwelling dynamics (Toggweiler et al., 2006; Watson et al., 2015) as well as alterations in Southern Ocean stratification (Hasenfrantz et al., 2019; Hines et al., 2024).

3.6. Deep circulation and water-mass geometry

Changes in the strength or geometry of deep circulation, and thus the composition of deep waters relative to the core site, could influence $\Delta\delta^{13}C_{(sub\text{-}deep)}$ independently of changes in iron or overlying productivity. This would result in deviations from a relationship between $\Delta\delta^{13}C_{(sub\text{-}deep)}$ and CO_2 or SAZ iron fluxes (Figure 6). For example, the canonical view of the glacial overturning circulation posits that the boundary between Northern Source Water (NSW, glacial equivalent of NADW) and Southern Source Water (SSW; a glacial analogue for CDW and AABW) shoaled by up to 500 m compared to interglacials conditions (e.g. Curry & Oppo, 2005). This shoaling of the NSW-SSW boundary at the AP_{comp} would expose benthic species to more depleted (lower $\delta^{13}C$) SSW, resulting in an increased $\Delta\delta^{13}C_{(sub\text{-}deep)}$. This scenario presents two pivotal questions: firstly could the shoaling of NSW and the enhanced presence of SSW during glacials of Interval I compared to Interval II (i.e. the Early-Middle Pleistocene Transition) have contributed to the observed increase in glacial $\Delta\delta^{13}C_{(sub\text{-}deep)}$ (Figure 5, 6)? Secondly, could a subsequent deepening of nutrient/CO_2 rich waters between Intervals II and III account for the return to pre-MPT glacial $\Delta\delta^{13}C_{(sub\text{-}deep)}$ levels during the Late Pleistocene? In relation to the transition from Interval I to II, nutrient concentrations and carbon inventory in the deep south Atlantic likely increased by ~0.90 Ma, possibly driven by a greater influence of SSW at the expense of NSW, alongside increased mid-depth density stratification (Farmer et al., 2019; Hines et al., 2024). However, the subsequent return to pre-MPT glacial $\Delta\delta^{13}C_{(sub\text{-}deep)}$ levels remains more equivocal. Quasi-conservative reconstructions of deep-water provenance using authigenic εNd indicate similar glacial deep water mass geometry in the deep Atlantic between Interval II and Interval III (Kim et al., 2021; Lang et al., 2016). For instance, εNd values in the deep North Atlantic are comparable during MIS 2 and MIS 12 (εNd ~ -11), yet $\Delta\delta^{13}C_{(sub\text{-}deep)}$ is nearly 0.6‰ higher during MIS 12 compared to MIS 2 (Figure 5).

One possible explanation is that, despite modest shifts in water mass geometries, nutrient deepening intensified during the transition to the late Pleistocene such that the AP_{comp} (~2700 m water depth) no longer reflected the most isotopically depleted deep carbon pool during glaciation. Hodell et al. (2003) provided a $\Delta\delta^{13}C_{(intermediate\text{-}deep)}$ record based on benthic $\delta^{13}C$ data from ODP Site 1088 (intermediate depth; 2082 m) and ODP Site 1090 (deep; 3702 m), showing a decoupling from atmospheric CO_2 levels between intervals II and III, similar to our findings. However, if one replaced the benthic record from the 'deep' ODP Site 1090 data with the 'abyssal' ODP Site 1089 data (4621 m water depth), the resulting $\Delta\delta^{13}C$ gradient would be consistently higher during the last glacial period, indicating that the decoupling from CO_2 diminishes. If nutrient deepening during glaciations played a role, it suggests that the abyssal carbon pool during the Late Pleistocene was deeper than ~3700 m, supporting theories of increased density stratification and the development of a cold-salty abyssal South Atlantic (Adkins et al., 2002; Knorr et al., 2021). If this is accurate, our measurements likely underestimate the true $\Delta\delta^{13}C_{(intermediate\text{-}deep)}$ during late Pleistocene glaciations, serving as a minimum estimate. However, unfortunately the available record (ODP Site 1089) is not long enough to evaluate how these dynamics evolved across the MPT.

Nonetheless, the evidence for abyssal nutrient and carbon deepening, along with a stronger chemocline, during the late Pleistocene remains uncertain. This uncertainty mainly stems from ongoing challenges in accurately depicting bottom water isotope gradients. For example, Hodell et al. (2003) show a similar $\Delta\delta^{13}C_{(intermediate\text{-}deep)}$ evolution between ODP Site 1088 and both ODP Sites 1090 and 1089 when analysing the benthic foraminiferal species *Cibicidoides kullenbergi.* However, results differ over the last glacial cycle if *C. wuellerstorfi is* used instead*,* suggesting that the deep $\delta^{13}C$ signal may reflect species-specific responses to late Pleistocene glacial conditions, rather than changes in water mass gradients. Gottschalk et al. (2016) examine this further, revealing a systematic offset in the $\delta^{13}C$ values of *C. kullenbergi* and *C. wuellerstorfi* (the benthic species used in this study) in the deep Atlantic Southern Ocean. They note that *C. wuellerstorfi* is ~0.76 ± 0.44‰ heavier during the last glacial period. Therefore, while some evidence points to increased abyssal carbon storage (lower benthic $\delta^{13}C$) below the water depth of our site, which would counter the apparent late Pleistocene decoupling between $\Delta\delta^{13}C_{(sub\text{-}deep)}$ and glacial atmospheric CO_2, confirming this requires further $\delta^{13}C$ data from *C. wuellerstorfi* at deeper locations.

Crucially, our main findings depend on the relative vertical gradient ($\Delta\delta^{13}C$ between *G. truncatulinoides* and *C. wuellerstorfi*), rather than on absolute benthic $\delta^{13}C$ values. Since measurements of both planktic and benthic foraminifera were made on co-occurring samples and the same benthic species was consistently used throughout the record, any species-specific offset should remain effectively constant, thus not biasing the temporal trends or comparisons between glacial periods. We emphasise that future work, including species-specific calibrations and more detailed records from deeper sites (> 3700 m) of both *C. kullenbergi* and *C. wuellerstorfi*, are needed to better refine interpretations of abyssal carbon storage and the 'true' vertical structure of the $\Delta\delta^{13}C_{(sub\text{-}deep)}$ gradient and its evolution across the MPT.

3.7. Deglacial chemocline breakdowns in the Early-Middle Pleistocene

During Late Pleistocene glacial terminations, abrupt negative excursions in both the $\delta^{13}C$ of atmospheric CO_2 (Bauska et al., 2016) and upper ocean $\delta^{13}C$ records have been associated with the upwelling and outgassing of isotopically depleted CDW in the Southern Ocean (Menviel et al., 2018; Spero & Lea, 2002). This low $\delta^{13}C$ carbon was rapidly transferred to the SAZ and subtropical basins through northward Ekman circulation, alongside the formation of SAMW and AAIW, thereby propagating the $\delta^{13}C$ minima at least as far as the Southern Ocean intermediate waters that ventilate the thermocline (Jones et al., 2016). Additionally, air-sea exchange with the isotopically depleted CO_2 likely further propagated this signal. Conversely, the cause of $\delta^{13}C$ minima observed in the intermediate Atlantic (1000-2000m) have also been linked to temperature-dependent fractionation (Lynch-Stieglitz, 2019), a weakened biological pump (Menviel et al., 2015), and a weakened AMOC (Oppo et al., 2015). The upwelling of respired carbon that CIMEs likely indicate plays a central role in the hypothesized sequence of events surrounding Late Pleistocene glacial terminations. For example, Denton et al. (2010) propose that the rapidity of the Last Deglaciation can be partially explained by the collapse of large Northern Hemisphere ice sheets, which initiated stadial conditions, forcing the Southern Hemisphere westerly winds southwards, thus enhancing CDW upwelling and subsequently releasing CO_2, ultimately leading to interglacial conditions.

Little, if any, previous work has investigated whether deglacial CIMEs developed across the MPT and are therefore unique to the Pleistocene and intense glacials. In addition to identifying a CIME during Termination I (TI, ca. 18 ka), Ziegler *et al*. (2013) documented further chemocline breakdowns during TII (ca. 130 ka), TIII (ca. 235 ka), and a more muted event during TIV (ca. 330

ka). Our new $\Delta\delta^{13}C_{(sub\text{-}deep)}$ record indicates chemocline breakdowns during multiple deglaciations, extending back to at least MIS 54 (Figure 4). Consistent with the mechanisms proposed for TI (i.e. Spero and Lea, 2002), the $\Delta\delta^{13}C_{(sub\text{-}deep)}$ values approaching zero generally align with peaks in the nutrient supply from AAZ (Figure 4; Ba/Fe from ODP Site 1094; Jaccard et al., 2013) and opal productivity (Tang et al., 2016), as well as minima in AP_{comp} near-bottom flow speed, which serves as a proxy for the meridional position and/or strength of the Antarctic Circumpolar Current (ACC; Starr *et al*., 2025) (Figure 4). Furthermore, a notable correlation exists between the occurrence and intensity of deglacial $\Delta\delta^{13}C_{(sub\text{-}deep)}$ minima and Ba/Fe peaks in the AAZ (Jaccard et al., 2013), although we note that the controls on Antarctic Zone productivity in the Early Pleistocene are poorly constrained. For example, more pronounced deglacial chemocline breakdowns following the Mid-Brunhes Event (~430 ka) coincide with intensified deglacial Ba/Fe peaks and flow speed minima compared to the preceding intervals.

Despite the challenges posed by variable sedimentation rates, $\Delta\delta^{13}C_{(sub\text{-}deep)}$ values nearing zero have been documented as far back as TXXIV (ca. 1.52 Ma). Moreover, the magnitude of deglacial $\Delta\delta^{13}C_{(sub\text{-}deep)}$ minima is broadly similar before and after the MPT, although the pre-MPT minima were shorter lived, suggesting that glacial-interglacial transitions within the 41-kyr world were also associated with the upwelling of isotopically depleted deep waters. Consequently, the transfer of CO_2 from the deep ocean into the atmosphere occurring during all deglaciations, both pre- and post-MPT, is characterised by the breakdown in SO stratification and carbon leakage from the deep ocean to the upper ocean in this region. Moreover, the observed relationship between chemocline breakdowns and poleward contractions in the ACC south of Africa (Starr *et al*., *2025*) implies a consistent link between deglacial upwelling and the Southern Ocean circumpolar circulation, as suggested for the Late Pleistocene (Denton et al., 2010; Toggweiler et al., 2006). However, we recognise that additional studies into potential drivers of deglacial $\Delta\delta^{13}C_{(sub\text{-}deep)}$ minima in the Early Pleistocene, such as air-sea exchange, weakened stratification or biological pump, terrestrial carbon release, are necessary to establish a definitive connection between wind-driven upwelling and our carbon isotope record.

5 Conclusions

In summary, we propose that the increase in glacial $\Delta\delta^{13}C_{(sub\text{-}deep)}$ during the early MPT (Intervals I to II) may be attributed to an increasingly efficient biological pump, possibly stimulated by SAZ iron fertilisation (Chalk et al., 2017). Conversely, the subsequent reduction in glacial $\Delta\delta^{13}C_{(sub\text{-}deep)}$ post-MIS 10 (Intervals II to III) demonstrates that this change is not attributable to shifts in biological pump efficiency. A northern expansion of the SAZ during glacials across this interval would have shifted the position of the AP_{comp} in relation to the meridional profiles of $\Delta\delta^{13}C_{(sub\text{-}deep)}$ and $\Delta\delta^{18}O_{(sub\text{-}deep)}$ south of Africa (Figure 7). If correct, this alteration in $\Delta\delta^{13}C_{(sub\text{-}deep)}$ could occur independently of a change in Southern Ocean nutrient utilization or air-sea exchange, both of which would likely influence glacial CO_2 levels. Non-stationarity would then explain the apparent decoupling between $\Delta\delta^{13}C_{(sub\text{-}deep)}$ and atmospheric CO_2, and SAZ iron fluxes during the Late Pleistocene. Additionally, the near-bottom flow speed record from the AP_{comp} (Figure 4; Starr *et al*., 2025) shows a consistent increasing trend in the proximity or strength of the ACC, specifically the SAF, during glacials following MIS 10. An increasingly proximal ACC SAF jet is expected with the expansion of the SAZ during this period. However, the support for a long-term SST shift in the Southern Hemisphere extra-tropical regions after MIS 10 remains equivocal. Clark et al. (2024) reveal no significant cooling in mean SH extratropical SST during this period, while the ODP Site 1090 (Martínez-Garcia et al., 2011) and AP_{comp} (Cartagena-Sierra et al., 2021; Romero et al., 2015; Tangunan et al., 2021) SST records suggest only a minor cooling (Figure S3).

It is evident that additional quantitative reconstructions of the Southern Ocean's expansion and contraction during the Early and Middle Pleistocene are essential. These efforts should mirror those utilised for the LGM (Gray et al., 2023; Kohfeld et al., 2013). Likewise, acquiring new, long-term records of $\Delta\delta^{13}C_{(sub\text{-}deep)}$ from locations outside of the SAZ, such as the Southern Hemisphere subtropical gyres, will be crucial to confirm the full strength of the chemocline and the degree to which it explains the evolution of Pleistocene glacial atmospheric CO_2 levels. Regardless of the drivers of these long-term changes, the collapse of the chemocline is likely systematically linked to deglaciation and the rise in atmospheric CO_2, occurring during short, moderate, and longer, more severe glacial periods in both pre- and post-MPT worlds.

Acknowledgments

The authors declare that they have no competing interests.This research used samples and/or data provided by the International Ocean Discovery Program (IODP). Funding for this research was provided by The Natural Environmental Research Council GW4+ DTP and NERC Grant NE/P000037/1. The authors thank Miros Charidemou for his assistance in the laboratory. We are grateful to the reviewers for their constructive comments on the manuscript and the suggestions that helped us improve it.

Open Research

Code Availability

Python code to reproduce the analysis will be archived at Zenodo.org.

Data Availability

All newly generated data will be made available through Pangaea.de.

Conflict of interest

The authors declare there are no conflicts of interest for this manuscript.

References

Adkins, J. F., McIntyre, K., & Schrag, D. P. (2002). The Salinity, Temperature, and δ^{18}O of the Glacial Deep Ocean. *Science*, *298* (5599), 1769–1773. https://doi.org/10.1126/science.1076252

Ahn, S., Khider, D., Lisiecki, L. E., & Lawrence, C. E. (2017). A probabilistic Pliocene–Pleistocene stack of benthic δ^{18}O using a profile hidden Markov model. *Dynamics and Statistics of the Climate System*, *2*(1). https://doi.org/10.1093/climsys/dzx002

An, Z., Zhou, W., Zhang, Z., Zhang, X., Liu, Z., Sun, Y., et al. (2024). Mid-Pleistocene climate transition triggered by Antarctic Ice Sheet growth. *Science*, *385*(6708), 560–565. https://doi.org/10.1126/science.abn4861

Anderson, R. F., Barker, S., Fleisher, M., Gersonde, R., Goldstein, S. L., Kuhn, G., et al. (2014). Biological response to millennial variability of dust and nutrient supply in the Subantarctic South Atlantic Ocean. *Philosophical Transactions of the Royal Society A: Mathematical, Physical and Engineering Sciences*, *372*, 20130054. https://doi.org/10.1098/rsta.2013.0054

Bauska, T. K., Baggenstos, D., Brook, E. J., Mix, A. C., Marcott, S. A., Petrenko, V. V., et al. (2016). Carbon isotopes characterize rapid changes in atmospheric carbon dioxide during the last deglaciation. *Proceedings of the National Academy of Sciences*, *113*(13), 3465–3470. https://doi.org/10.1073/pnas.1513868113

Becquey, S., & Gersonde, R. (2002). Past hydrographic and climatic changes in the Subantarctic Zone of the South Atlantic – The Pleistocene record from ODP Site 1090. *Palaeogeography, Palaeoclimatology, Palaeoecology*, *182*(3–4), 221–239. https://doi.org/10.1016/S0031-0182(01)00497-7

Bereiter, B., Eggleston, S., Schmitt, J., Nehrbass-Ahles, C., Stocker, T. F., Fischer, H., et al. (2015). Revision of the EPICA Dome C CO_2 record from 800 to 600 kyr before present. *Geophysical Research Letters*, *42*(2), 542–549. https://doi.org/10.1002/2014GL061957

Berger, W. H., Kroenke, L. W., Mayer, L. A., & et al. (Eds.). (1993). *Proceedings of the Ocean Drilling Program, 130 Scientific Results* (Vol. 130). Ocean Drilling Program. https://doi.org/10.2973/odp.proc.sr.130.1993

Bolton, C. T., Chang, L., Clemens, S. C., Kodama, K., Ikehara, M., Medina-Elizalde, M., et al. (2013). A 500,000 year record of Indian summer monsoon dynamics recorded by eastern equatorial Indian Ocean upper water-column structure. *Quaternary Science Reviews*, *77*, 167–180. https://doi.org/10.1016/j.quascirev.2013.07.031

Bower, A., Lozier, S., Biastoch, A., Drouin, K., Foukal, N., Furey, H., et al. (2019). Lagrangian Views of the Pathways of the Atlantic Meridional Overturning Circulation. *Journal of Geophysical Research: Oceans*, *124*(8), 5313–5335. https://doi.org/10.1029/2019JC015014

Broecker, W. S. (1982). Ocean chemistry during glacial time. *Geochimica et Cosmochimica Acta*, *46*(10), 1689–1705. https://doi.org/10.1016/0016-7037(82)90110-7

Cartagena-Sierra, A., Berke, M. A., Robinson, R. S., Marcks, B., Castañeda, I. S., Starr, A., et al. (2021). Latitudinal Migrations of the Subtropical Front at the Agulhas Plateau Through the Mid-Pleistocene Transition. *Paleoceanography and Paleoclimatology*, *36*(7), e2020PA004084. https://doi.org/10.1029/2020PA004084

Chalk, T. B., Hain, M. P., Foster, G. L., Rohling, E. J., Sexton, P. F., Badger, M. P. S., et al. (2017). Causes of ice age intensification across the Mid-Pleistocene Transition. *Proceedings of the National Academy of Sciences*, *114*(50), 13114–13119. https://doi.org/10.1073/pnas.1702143114

Charles, C. D., Wright, J. D., & Fairbanks, R. G. (1993). Thermodynamic influences on the marine carbon isotope record. *Paleoceanography*, *8*(6), 691–697. https://doi.org/10.1029/93PA01803

Charles, C. D., Pahnke, K., Zahn, R., Mortyn, P. G., Ninnemann, U., & Hodell, D. A. (2010). Millennial scale evolution of the Southern Ocean chemical divide. *Quaternary Science Reviews*, *29*(3–4), 399–409. https://doi.org/10.1016/j.quascirev.2009.09.021

Chiessi, C. M., Ulrich, S., Mulitza, S., Pätzold, J., & Wefer, G. (2007). Signature of the Brazil-Malvinas Confluence (Argentine Basin) in the isotopic composition of planktonic foraminifera from surface sediments. *Marine Micropaleontology*, *64*(1–2), 52–66. https://doi.org/10.1016/j.marmicro.2007.02.002

Clark, P. U., & Pollard, D. (1998). Origin of the Middle Pleistocene Transition by ice sheet erosion of regolith. *Paleoceanography*, *13*(1), 1–9. https://doi.org/10.1029/97PA02660

Clark, P. U., Shakun, J. D., Rosenthal, Y., Köhler, P., & Bartlein, P. J. (2024). Global and regional temperature change over the past 4.5 million years. *Science*, *383*(6685), 884–890. https://doi.org/10.1126/science.adi1908

Curry, W. B., & Oppo, D. W. (2005). Glacial water mass geometry and the distribution of $\delta^{13}C$ of ΣCO_2 in the western Atlantic Ocean. *Paleoceanography*, *20*(1), 2004PA001021. https://doi.org/10.1029/2004PA001021

Curry, William B., & Crowley, T. J. (1987). The $\delta^{13}C$ of equatorial Atlantic surface waters: Implications for Ice Age pCO_2 levels. *Paleoceanography*, *2*(5), 489–517. https://doi.org/10.1029/PA002i005p00489

Denton, G. H., Anderson, R. F., Toggweiler, J. R., Edwards, R. L., Schaefer, J. M., & Putnam, A. E. (2010). The Last Glacial Termination. *Science*, *328*(5986), 1652–1656. https://doi.org/10.1126/science.1184119

Dyez, K. A., Hönisch, B., & Schmidt, G. A. (2018). Early Pleistocene Obliquity-Scale pCO_2 Variability at ~1.5 Million Years Ago. *Paleoceanography and Paleoclimatology*, *33*(11), 1270–1291. https://doi.org/10.1029/2018PA003349

Eide, M., Olsen, A., Ninnemann, U. S., & Johannessen, T. (2017). A global ocean climatology of preindustrial and modern ocean $\delta^{13}C$. *Global Biogeochemical Cycles*, *31*(3), 515–534. https://doi.org/10.1002/2016GB005473

Farmer, J. R., Hönisch, B., Haynes, L. L., Kroon, D., Jung, S., Ford, H. L., et al. (2019). Deep Atlantic Ocean carbon storage and the rise of 100,000-year glacial cycles. *Nature Geoscience*, 12(5), 355–360. https://doi.org/10.1038/s41561-019-0334-6

Ferrari, R., Jansen, M. F., Adkins, J. F., Burke, A., Stewart, A. L., & Thompson, A. F. (2014). Antarctic sea ice control on ocean circulation in present and glacial climates. *Proceedings of the National Academy of Sciences*, *111*(24), 8753–8758. https://doi.org/10.1073/pnas.1323922111

Foster, G. L. (2008). Seawater pH, pCO_2 and $[CO_2{}^{-3}]$ variations in the Caribbean Sea over the last 130 kyr: A boron isotope and B/Ca study of planktic foraminifera. *Earth and Planetary Science Letters*, 271(1–4), 254–266. https://doi.org/10.1016/j.epsl.2008.04.015

Fraass, A. J., & Lowery, C. M. (2017). Defining uncertainty and error in planktic foraminiferal oxygen isotope measurements. *Paleoceanography*, *32*(2), 104–122. https://doi.org/10.1002/2016PA003035

Galbraith, E. D., & Eggleston, S. (2017). A lower limit to atmospheric CO_2 concentrations over the past 800,000 years. *Nature Geoscience*, *10*(4), 295–298. https://doi.org/10.1038/ngeo2914

Gottschalk, J., Vázquez Riveiros, N., Waelbroeck, C., Skinner, L. C., Michel, E., Duplessy, J., et al. (2016). Carbon isotope offsets between benthic foraminifer species of the genus *Cibicides* (*Cibicidoides*) in the glacial sub-Antarctic Atlantic. *Paleoceanography*, *31*(12), 1583–1602. https://doi.org/10.1002/2016PA003029

Gray, W. R., De Lavergne, C., Jnglin Wills, R. C., Menviel, L., Spence, P., Holzer, M., et al. (2023). Poleward Shift in the Southern Hemisphere Westerly Winds Synchronous With the Deglacial Rise in CO_2. *Paleoceanography and Paleoclimatology*, *38*(7), e2023PA004666. https://doi.org/10.1029/2023PA004666

Hain, M. P., Sigman, D. M., & Haug, G. H. (2010). Carbon dioxide effects of Antarctic stratification, North Atlantic Intermediate Water formation, and subantarctic nutrient drawdown during the last ice age: Diagnosis and synthesis in a geochemical box model. *Global Biogeochemical Cycles*, *24*(4), 2010GB003790. https://doi.org/10.1029/2010GB003790

Hasenfratz, A. P., Jaccard, S. L., Martínez-García, A., Sigman, D. M., Hodell, D. A., Vance, D., et al. (2019). The residence time of Southern Ocean surface waters and the 100,000-year ice age cycle. *Science*, *363*(6431), 1080–1084. https://doi.org/10.1126/science.aat7067

Henehan, M. J., Rae, J. W. B., Foster, G. L., Erez, J., Prentice, K. C., Kucera, M., et al. (2013). Calibration of the boron isotope proxy in the planktonic foraminifera Globigerinoides ruber for use in palaeo-CO_2 reconstruction. *Earth and Planetary Science Letters*, *364*, 111–122. https://doi.org/10.1016/j.epsl.2012.12.029

Herbert, T. D. (2023). The Mid-Pleistocene Climate Transition. *Annual Review of Earth and Planetary Sciences*, *51*(1), 389–418. https://doi.org/10.1146/annurev-earth-032320-104209

Higgins, J. A., Kurbatov, A. V., Spaulding, N. E., Brook, E., Introne, D. S., Chimiak, L. M., et al. (2015). Atmospheric composition 1 million years ago from blue ice in the Allan Hills, Antarctica. *Proceedings of the National Academy of Sciences*, *112*(22), 6887–6891. https://doi.org/10.1073/pnas.1420232112

Hines, S. K.V., Charles, C.D., Starr, A., Goldstein, S. L., Hemming, S. R., Hall, I.R., et. al 2024. Revisiting the mid-Pleistocene transition ocean circulation crisis. *Science* 386 (6722), pp. 681-686. https://doi.org/10.1126/science.adn4154

Ho, S. L., Mollenhauer, G., Lamy, F., Martínez-Garcia, A., Mohtadi, M., Gersonde, R., et al. (2012). Sea surface temperature variability in the Pacific sector of the Southern Ocean over the past 700 kyr. *Paleoceanography*, *27*(4), 2012PA002317. https://doi.org/10.1029/2012PA002317

Hodell, D., Crowhurst, S., Lourens, L., Margari, V., Nicolson, J., Rolfe, J. E., et al. (2023). A 1.5-Million-Year Record of Orbital and Millennial Climate Variability in the North Atlantic. *Climate of the Past*, 19(3), 607-636. https://doi.org/10.5194/cp-19-607-202

Hodell, D. A., Venz, K. A., Charles, C. D., & Ninnemann, U. S. (2003). Pleistocene vertical carbon isotope and carbonate gradients in the South Atlantic sector of the Southern Ocean. *Geochemistry, Geophysics, Geosystems*, *4*(1), 1–19. https://doi.org/10.1029/2002GC000367

Hönisch, B., Hemming, N. G., Archer, D., Siddall, M., & McManus, J. F. (2009). Atmospheric Carbon Dioxide Concentration Across the Mid-Pleistocene Transition. *Science*, *324*(5934), 1551–1554. https://doi.org/10.1126/science.1171477

Hoogakker, B. A. A., Rohling, E. J., Palmer, M. R., Tyrrell, T., & Rothwell, R. G. (2006). Underlying causes for long-term global ocean δ^{13}C fluctuations over the last 1.20 Myr. *Earth and Planetary Science Letters*, *248*(1–2), 15–29. https://doi.org/10.1016/j.epsl.2006.05.007

Hu, R., Bostock, H. C., Greaves, M., Piotrowski, A. M., & McCave, I. N. (2020). Coupled evolution of stable carbon isotopes between the Southern Ocean and the atmosphere over the last 260 ka. *Earth and Planetary Science Letters*, *538*, 116215. https://doi.org/10.1016/j.epsl.2020.116215

Imbrie, J., Berger, A., Boyle, E. A., Clemens, S. C., Duffy, A., Howard, W. R., et al. (1993). On the structure and origin of major glaciation cycles 2. The 100,000-year cycle. *Paleoceanography*, *8*(6), 699–735. https://doi.org/10.1029/93PA02751

Jaccard, S. L., Hayes, C. T., Martinez-Garcia, A., Hodell, D. A., Anderson, R. F., Sigman, D. M., & Haug, G. H. (2013). Two Modes of Change in Southern Ocean Productivity Over the Past Million Years. *Science*, *339*(6126), 1419–1423. https://doi.org/10.1126/science.1227545

Jones, D. C., Meijers, A. J. S., Shuckburgh, E., Sallée, J.-B., Haynes, P., McAufield, E. K., & Mazloff, M. R. (2016). How does Subantarctic Mode Water ventilate the Southern Hemisphere subtropics?. *Journal of Geophysical Research: Oceans*, *121*(9), 6558–6582. https://doi.org/10.1002/2016JC011680

Kim, J., Goldstein, S. L., Pena, L. D., Jaume-Seguí, M., Knudson, K. P., Yehudai, M., & Bolge, L. (2021). North Atlantic Deep Water during Pleistocene interglacials and glacials. *Quaternary Science Reviews*, *269*, 107146. https://doi.org/10.1016/j.quascirev.2021.107146

Kim, S.-T., & O'Neil, J. R. (1997). Equilibrium and nonequilibrium oxygen isotope effects in synthetic carbonates. *Geochimica et Cosmochimica Acta*, *61*(16), 3461–3475. https://doi.org/10.1016/S0016-7037(97)00169-5

Knorr, G., Barker, S., Zhang, X., Lohmann, G., Gong, X., Gierz, P., et al. (2021). A salty deep ocean as a prerequisite for glacial termination. *Nature Geoscience*, *14*(12), 930–936. https://doi.org/10.1038/s41561-021-00857-3

Kohfeld, K. E., Graham, R. M., de Boer, A. M., Sime, L. C., Wolff, E. W., Le Quéré, C., & Bopp, L. (2013). Southern Hemisphere westerly wind changes during the Last Glacial Maximum: paleo-data synthesis. *Quaternary Science Reviews*, *68*, 76–95. https://doi.org/10.1016/j.quascirev.2013.01.017

Kroopnick, P. M. (1985). The distribution of ^{13}C of ΣCO_2 in the world oceans. *Deep Sea Research Part A. Oceanographic Research Papers*, *32*(1), 57–84. https://doi.org/10.1016/0198-0149(85)90017-2

Lambert, F., Tagliabue, A., Shaffer, G., Lamy, F., Winckler, G., Farias, L., et al. (2015). Dust fluxes and iron fertilization in Holocene and Last Glacial Maximum climates. *Geophysical Research Letters*, *42*(14), 6014–6023. https://doi.org/10.1002/2015GL064250

Lang, D. C., Bailey, I., Wilson, P. A., Chalk, T. B., Foster, G. L., & Gutjahr, M. (2016). Incursions of southern-sourced water into the deep North Atlantic during late Pliocene glacial intensification. *Nature Geoscience*, *9*(5), 375–379. https://doi.org/10.1038/ngeo2688

Laskar, J., Robutel, P., Joutel, F., Gastineau, M., Correia, A. C. M., & Levrard, B. (2004). A long-term numerical solution for the insolation quantities of the Earth. *Astronomy & Astrophysics*, *428*(1), 261–285. https://doi.org/10.1051/0004-6361:20041335

Lear, C. H., Billups, K., Rickaby, R. E. M., Diester-Haass, L., Mawbey, E. M., & Sosdian, S. M. (2016). Breathing more deeply: Deep ocean carbon storage during the mid-Pleistocene climate transition. *Geology*, *44*(12), 1035–1038. https://doi.org/10.1130/G38636.1

LeGrande, A. N., & Schmidt, G. A. (2006). Global gridded data set of the oxygen isotopic composition in seawater. *Geophysical Research Letters*, *33*(12), 2006GL026011. https://doi.org/10.1029/2006GL026011

Lisiecki, L. E., & Raymo, M. E. (2005). A Pliocene-Pleistocene stack of 57 globally distributed benthic δ^{18}O records: Pliocene-Pleistocene Benthic Stack. *Paleoceanography*, *20*(1), PA1003 https://doi.org/10.1029/2004PA001071

Locarnini, R. A., Mishonov, A. V., Baranova, O. K., Boyer, T. P., Zweng, M. M., & Smolyar, I. (2018). World Ocean Atlas 2018, Volume 1: Temperature. [Data set]. NOAA National Centers for Environmental Information. Retrieved from https://www.ncei.noaa.gov/archive/accession/NCEI-WOA18

Lynch-Stieglitz, J. (2019). Temperature-dependent ocean–atmosphere equilibration of carbon isotopes in surface and intermediate waters over the deglaciation. *Earth and Planetary Science Letters*, 506, 466-475. https://doi.org/10.1016/j.epsl.2018.11.024

Marchitto, T. M., Curry, W. B., Lynch-Stieglitz, J., Bryan, S. P., Cobb, K. M., & Lund, D. C. (2014). Improved oxygen isotope temperature calibrations for cosmopolitan benthic foraminifera. *Geochimica et Cosmochimica Acta*, *130*, 1–11. https://doi.org/10.1016/j.gca.2013.12.034

Marinov, I., Gnanadesikan, A., Toggweiler, J. R., & Sarmiento, J. L. (2006). The Southern Ocean biogeochemical divide. *Nature*, *441*(7096), 964–967. https://doi.org/10.1038/nature04883

Marshall, J., & Speer, K. (2012). Closure of the meridional overturning circulation through Southern Ocean upwelling. *Nature Geoscience*, *5*(3), 171–180. https://doi.org/10.1038/ngeo1391

Martin, J. H. (1990). Glacial-interglacial CO_2 change: The Iron Hypothesis. *Paleoceanography*, *5*(1), 1–13. https://doi.org/10.1029/PA005i001p00001

Martínez-Garcia, A., Rosell-Melé, A., Jaccard, S. L., Geibert, W., Sigman, D. M., & Haug, G. H. (2011). Southern Ocean dust–climate coupling over the past four million years. *Nature*, *476*(7360), 312–315. https://doi.org/10.1038/nature10310

Martínez-García, A., Sigman, D. M., Ren, H., Anderson, R. F., Straub, M., Hodell, D. A., et al. (2014). Iron Fertilization of the Subantarctic Ocean During the Last Ice Age. *Science*, *343*(6177), 1347–1350. https://doi.org/10.1126/science.1246848

McClymont, E. L., Elmore, A. C., Kender, S., Leng, M. J., Greaves, M., & Elderfield, H. (2016). Pliocene-Pleistocene evolution of sea surface and intermediate water temperatures from the southwest Pacific. *Paleoceanography*, *31*(6), 895–913. https://doi.org/10.1002/2016PA002954

Menviel, L., Mouchet, A., Meissner, K. J., Joos, F., & England, M. H. (2015). Impact of oceanic circulation changes on atmospheric $\delta^{13}CO_2$. *Global Biogeochemical Cycles*, *29*(11), 1944–1961. https://doi.org/10.1002/2015GB005207

Menviel, L., Spence, P., Yu, J., Chamberlain, M. A., Matear, R. J., Meissner, K. J., & England, M. H. (2018). Southern Hemisphere westerlies as a driver of the early deglacial atmospheric CO_2 rise. *Nature Communications*, *9*(1), 2503. https://doi.org/10.1038/s41467-018-04876-4

Mook, W. G., Bommerson, J. C., & Staverman, W. H. (1974). Carbon isotope fractionation between dissolved bicarbonate and gaseous carbon dioxide. *Earth and Planetary Science Letters*, *22*(2), 169–176. https://doi.org/10.1016/0012-821X(74)90078-8

Morée, A. L., Schwinger, J., & Heinze, C. (2018). Southern Ocean controls of the vertical marine δ^{13}C gradient – a modelling study. *Biogeosciences*, *15*(23), 7205–7223. https://doi.org/10.5194/bg-15-7205-2018

Murnane, R. J., & Sarmiento, J. L. (2000). Roles of biology and gas exchange in determining the δ^{13}C distribution in the ocean and the preindustrial gradient in atmospheric δ^{13}C. *Global Biogeochemical Cycles*, *14*(1), 389–405. https://doi.org/10.1029/1998GB001071

Nascimento, R.A., Santos, T., Venancio, I.M., Chiessi, C.M., Ballalai, J.M., Kuhnert, H., Govin, A., Portilho-Ramos, R.C., Lessa, D., Dias, B.B., Pinho, T.M., Crivellari, S., Mulitza, S., Albuquerque, A.L.S. (2021). Origin of δ^{13}C minimum events in thermocline and intermediate waters of the western South Atlantic. *Quaternary Science Reviews*, 272, 107224, https://doi.org/10.1016/j.quascirev.2021.107224

Ninnemann, U. S., & Charles, C. D. (1997). Regional differences in Quaternary subantarctic nutrient cycling: Link to intermediate and deep water ventilation. *Paleoceanography*, *12*(4), 560–567. https://doi.org/10.1029/97PA01032

Oppo, D. W., & Fairbanks, R. G. (1989). Carbon isotope composition of tropical surface water during the past 22,000 years. *Paleoceanography*, *4*(4), 333–351. https://doi.org/10.1029/PA004i004p00333

Oppo, D. W., Curry, W. B., & McManus, J. F. (2015). What do benthic δ^{13}C and δ^{18}O data tell us about Atlantic circulation during Heinrich Stadial 1? *Paleoceanography*, *30*(4), 353–368. https://doi.org/10.1002/2014PA002667

Park, Y. -H., Park, T., Kim, T. -W., Lee, S. -H., Hong, C. -S., Lee, J. -H., et al. (2019). Observations of the Antarctic Circumpolar Current Over the Udintsev Fracture Zone, the Narrowest Choke Point in the Southern Ocean. *Journal of Geophysical Research: Oceans*, *124*(7), 4511–4528. https://doi.org/10.1029/2019JC015024

Primeau, F. W., Holzer, M., & DeVries, T. (2013). Southern Ocean nutrient trapping and the efficiency of the biological pump. *Journal of Geophysical Research: Oceans*, *118*(5), 2547–2564. https://doi.org/10.1002/jgrc.20181

Quillévéré, F., Morard, R., Escarguel, G., Douady, C. J., Ujiié, Y., De Garidel-Thoron, T., & De Vargas, C. (2013). Global scale same-specimen morpho-genetic analysis of Truncorotalia truncatulinoides: A perspective on the morphological species concept in planktonic foraminifera. *Palaeogeography, Palaeoclimatology, Palaeoecology*, *391*, 2–12. https://doi.org/10.1016/j.palaeo.2011.03.013

Raymo, M. E., Ruddiman, W. F. & Froelich, P. N. (1998). Influence of late Cenozoic Mountain building on ocean geochemical cycles. *Geology* 16, 649–653.

https://doi.org/10.1130/0091-7613(1988)016<0649:IOLCMB>2.3.CO;2

Romahn, S., Mackensen, A., Groeneveld, J., & Pätzold, J. (2014). Deglacial intermediate water reorganization: new evidence from the Indian Ocean. *Climate of the Past*, *10*(1), 293–303. https://doi.org/10.5194/cp-10-293-2014

Romero, O. E., Kim, J.-H., Bárcena, M. A., Hall, I. R., Zahn, R., & Schneider, R. (2015). High-latitude forcing of diatom productivity in the southern Agulhas Plateau during the past 350 kyr: Late Pleistocene diatom productivity. *Paleoceanography*, *30*(2), 118–132. https://doi.org/10.1002/2014PA002636

Sallée, J.-B., Speer, K., Rintoul, S., & Wijffels, S. (2010). Southern Ocean Thermocline Ventilation. *Journal of Physical Oceanography*, *40*(3), 509–529. https://doi.org/10.1175/2009JPO4291.1

Scussolini, P., and Peeters, F.J.C. (2013). A record of the last 460 thousand years of upper ocean stratification from the central Walvis Ridge, South Atlantic. *Paleoceanography* 28(3), 426-439.

Sexton, P. F., & Norris, R. D. (2008). Dispersal and biogeography of marine plankton: Long-distance dispersal of the foraminifer Truncorotalia truncatulinoides. *Geology*, *36*(11), 899. https://doi.org/10.1130/G25232A.1

Shao, J., Stott, L. D., Menviel, L., Ridgwell, A., Ödalen, M., & Mohtadi, M. (2021). The atmospheric bridge communicated the δ^{13}C decline during the last deglaciation to the global upper ocean. *Climate of the Past*, *17*(4), 1507–1521. https://doi.org/10.5194/cp-17-1507-2021

Shoenfelt, E. M., Winckler, G., Lamy, F., Anderson, R. F., & Bostick, B. C. (2018). Highly bioavailable dust-borne iron delivered to the Southern Ocean during glacial periods. *Proceedings of the National Academy of Sciences*, *115*(44), 11180–11185. https://doi.org/10.1073/pnas.1809755115

Sigman, D. M., & Boyle, E. A. (2000). Glacial/interglacial variations in atmospheric carbon dioxide. *Nature*, *407*(6806), 859–869. https://doi.org/10.1038/35038000

Spero, H. J., & Lea, D. W. (2002). The Cause of Carbon Isotope Minimum Events on Glacial Terminations. *Science*, *296*(5567), 522–525. https://doi.org/10.1126/science.1069401

Starr, A., Hall, I. R., Barker, S., Rackow, T., Zhang, X., Hemming, S. R., et al. (2021). Antarctic icebergs reorganize ocean circulation during Pleistocene glacials. *Nature*, *589*(7841), 236–241. https://doi.org/10.1038/s41586-020-03094-7

Stephens, B. B., & Keeling, R. F. (2000). The influence of Antarctic sea ice on glacial–interglacial CO2 variations. *Nature*, *404*(6774), 171–174. https://doi.org/10.1038/35004556

Talley, L. (2013). Closure of the Global Overturning Circulation Through the Indian, Pacific, and Southern Oceans: Schematics and Transports. *Oceanography*, *26*(1), 80–97. https://doi.org/10.5670/oceanog.2013.07

Tang, Z., Shi, X., Zhang, X., Chen, Z., Chen, M.-T., Wang, X., et al. (2016). Deglacial biogenic opal peaks revealing enhanced Southern Ocean upwelling during the last 513 ka. *Quaternary International*, *425*, 445–452. https://doi.org/10.1016/j.quaint.2016.09.020

Tangunan, D., Berke, M. A., Cartagena-Sierra, A., Flores, J. A., Gruetzner, J., Jiménez-Espejo, F., et al. (2021). Strong glacial-interglacial variability in upper ocean hydrodynamics, biogeochemistry, and productivity in the southern Indian Ocean. *Communications Earth & Environment*, *2*(1), 80. https://doi.org/10.1038/s43247-021-00148-0

Toggweiler, J. R. (1999). Variation of atmospheric CO $_2$ by ventilation of the ocean's deepest water. *Paleoceanography*, *14*(5), 571–588. https://doi.org/10.1029/1999PA900033

Toggweiler, J. R., Russell, J. L., & Carson, S. R. (2006). Midlatitude westerlies, atmospheric CO_2 , and climate change during the ice ages. *Paleoceanography*, *21*(2). https://doi.org/10.1029/2005PA001154

Tzedakis, P. C., Raynaud, D., McManus, J. F., Berger, A., Brovkin, V., & Kiefer, T. (2009). Interglacial diversity. *Nature Geoscience*, *2*(11), 751–755. https://doi.org/10.1038/ngeo660

Tzedakis, P. C., Crucifix, M., Mitsui, T., & Wolff, E. W. (2017). A simple rule to determine which insolation cycles lead to interglacials. *Nature*, *542*(7642), 427–432. https://doi.org/10.1038/nature21364

Uemura, R., Motoyama, H., Masson-Delmotte, V., Jouzel, J., Kawamura, K., Goto-Azuma, K., et al. (2018). Asynchrony between Antarctic temperature and CO_2 associated with obliquity over the past 720,000 years. *Nature Communications*, *9*(1), 961. https://doi.org/10.1038/s41467-018-03328-3

Wang, P., Tian, J., & Lourens, L. J. (2010). Obscuring of long eccentricity cyclicity in Pleistocene oceanic carbon isotope records. *Earth and Planetary Science Letters*, *290*(3–4), 319–330. https://doi.org/10.1016/j.epsl.2009.12.028

Waskom, M. L. (2021). Seaborn: Statistical data visualization. *Journal of Open Source Software*, *6*(60), 3021. https://doi.org/10.21105/joss.03021

Watson, A., Vallis, G. K., & Nikurashin, M. (2015). Southern Ocean buoyancy forcing of ocean ventilation and glacial atmospheric CO_2. *Nature Geoscience*, 8(11), 861-864. https://doi.org/10.1038/ngeo2538

Weis, J., Chase, Z., Schallenberg, C., Strutton, P. G., Bowie, A. R., & Fiddes, S. L. (2024). One-third of Southern Ocean productivity is supported by dust deposition. *Nature*, *629*(8012), 603–608. https://doi.org/10.1038/s41586-024-07366-4

Willeit, M., Ganopolski, A., Calov, R., & Brovkin, V. (2019). Mid-Pleistocene transition in glacial cycles explained by declining CO_2 and regolith removal. *Science Advances*, *5*(4), eaav7337. https://doi.org/10.1126/sciadv.aav7337

Ziegler, M., Diz, P., Hall, I. R., & Zahn, R. (2013). Millennial-scale changes in atmospheric CO_2 levels linked to the Southern Ocean carbon isotope gradient and dust flux. *Nature Geoscience*, *6*(6), 457–461. https://doi.org/10.1038/ngeo1782

Table 1. Average glacial proxy values for $\Delta\delta^{13}C_{(sub\text{-}deep)}$ (this study), atmospheric CO_2 (compiled ice core and boron isotope proxy reconstructions, see text for full reference list), ODP Site 1090 Fe accumulation rate (Martínez-Garcia et al., 2011) and $\Delta\delta^{18}O_{(sub\text{-}deep)}$ (this study). Averages are taken of all glacial samples (i.e. samples that pass the two criteria outlined in the main text) from the three given intervals. Errors are estimated from bootstrap and gaussian resampling.

Interval	MIS range	$\Delta\delta^{13}C_{(sub\text{-}deep)}$ (‰) (Average)	$\Delta\delta^{13}C_{(sub\text{-}deep)}$ (‰) (Max. Intensity)	CO_2 (ppm)	Fe (mg/m^2/yr)	$\Delta\delta^{18}O_{(sub\text{-}deep)}$ (‰)
I	56 – 31	0.68 ± 0.02	1.05 ± 0.17	249.8 ± 2.6	146.6 ± 0.9	-1.86 ± 0.02
II	30 – 10	0.86 ± 0.01	1.29 ± 0.15	208.3 ± 0.8	268.2 ± 1.0	-1.71 ± 0.01
III	9 – 1	0.65 ± 0.01	0.95 ± 0.11	202.4 ± 0.3	257.0 ± 1.9	-1.35 ± 0.01

Figure 1. Core site and hydrographic context. (a) Map of annual mean Sea Surface Temperature (SST) from World Ocean Atlas 2018 (Locarnini et al., 2018) with core location references in the text. The red, yellow, and black contours represent the Subtropical Front (STF), Subantarctic Front (SAF), and Polar Front (PF), respectively (following (Park et al., 2019)). The zones between each front are labelled: SAZ = Subantarctic Zone; PFZ = Polar Frontal Zone; AAZ = Antarctic Zone. (b) North-south transect at 25ºE (red dashed line in (a)) of modern $\delta^{13}C$ of DIC (Suess-corrected data from Eide *et al*., 2017). White symbols denote approximate calcification ranges for G. truncatulinoides (triangle) and C. wuellerstorfi. (circle) Red text denotes key water masses: LCDW = Lower Circumpolar Deep Water; NADW = North Atlantic Deep Water; UCDW = Upper Circumpolar Deep Water; AASW = Antarctic Surface Water; SAMW = Subantarctic Mode Water; AAIW = Antarctic Intermediate Water. The yellow star shows the location of the Agulhas Plateau Composite (APcomp) core site (this study).

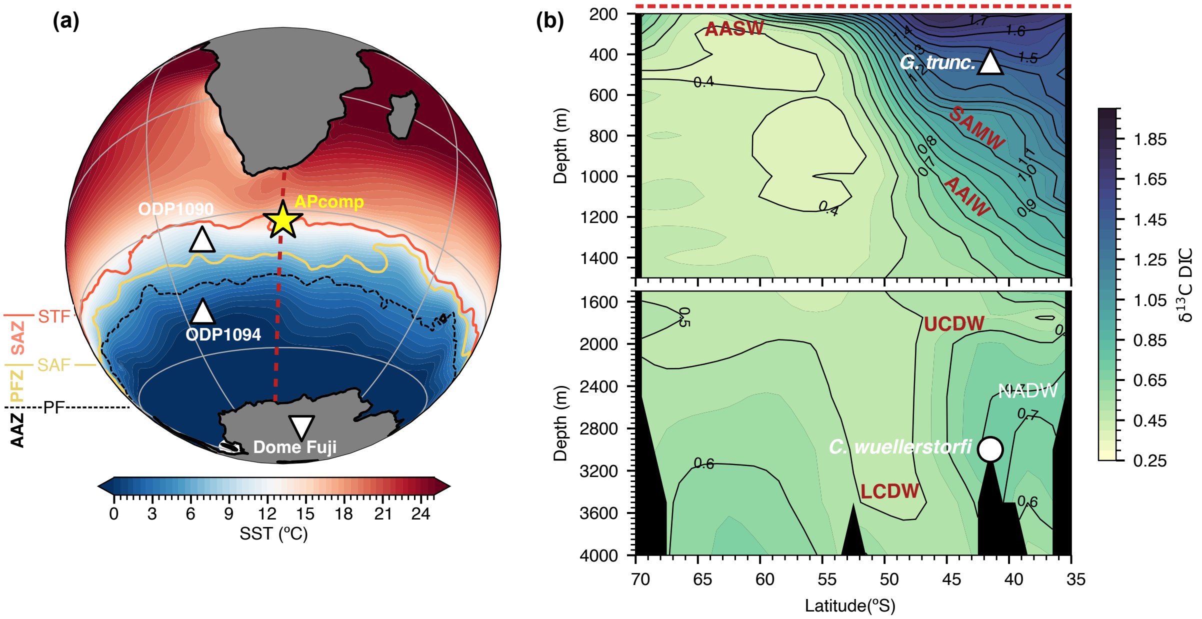

Figure 2. Individual Foraminifera Analysis (IFA) results. (a) Histogram of δ^{18}O measured on individual shells across 4 AP$_{comp}$ samples (with means removed). (b) same as (a) but for δ^{13}C. (c) Empirically derived standard error of the mean (SEM) for δ^{18}O and δ^{13}C, depending on the number of individual shells included in a measurement.

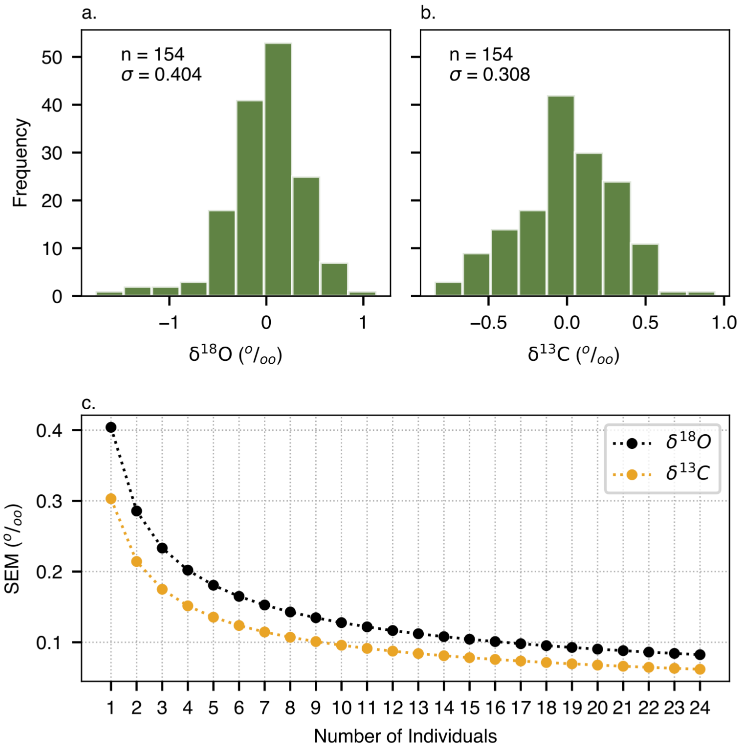

Figure 3. Downcore results. (a) benthic $\delta^{18}O$ from the AP_{comp} (Starr et al., 2021; Ziegler et al., 2013). (b) $\delta^{13}C$ data from *C. wuellerstorfi* (light teal) and *G. truncatulinoides* (dark green; error bars represent ± 1 ⌠). Lighter green (upper 300 ka) are data from Ziegler et al. (2013) (c) $\Delta\delta^{13}C_{(sub\text{-}deep)}$ from the AP_{comp} with ± 2 ⌠ uncertainty shaded. (d) Reconstructed atmospheric CO_2 levels from Antarctic ice cores (Black; Bereiter et al., 2015) and boron-isotope reconstructions (Chalk et al., 2017; Dyez et al., 2018; Foster, 2008; Henehan et al., 2013). The blue shaded data represents "Blue Ice" from Allan Hills (Higgins et al., 2015), with approximate age uncertainty shaded. (e) Fe accumulation rate from ODP Site 1090 in the Atlantic Subantarctic Zone (Martínez-Garcia et al., 2011).

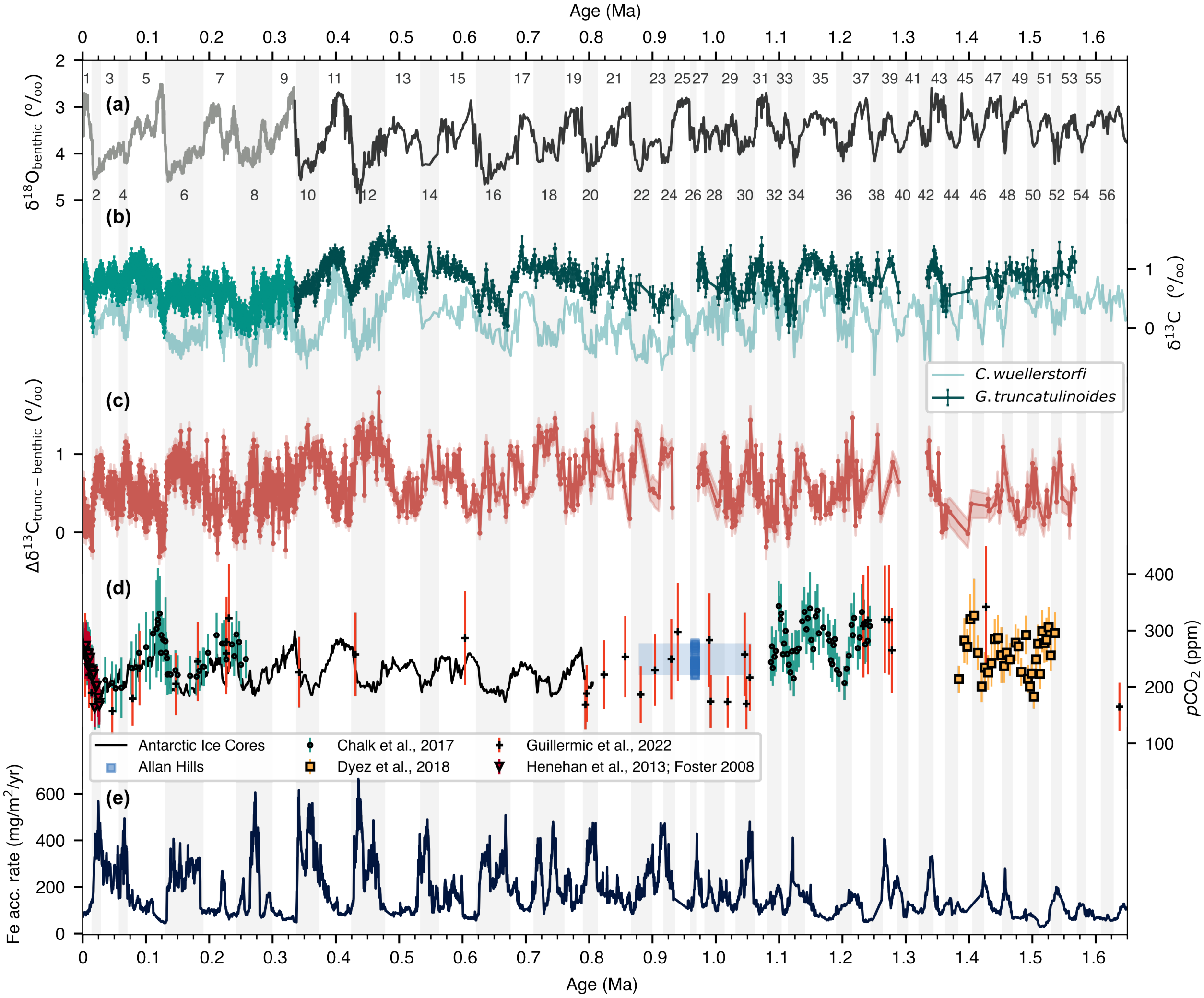

Figure 4. Glacial terminations. (a) Angle of obliquity (black line) and precession index (orange line) through time (Laskar et al., 2004). (b) AP_{comp} benthic $\delta^{18}O$ (Starr et al., 2021; Ziegler et al., 2013). (c) First derivative of a global benthic $\delta^{18}O$ stack (Ahn et al., 2017) where red (blue) shaded areas represent decreasing (increasing) $\delta^{18}O$ values and thus deglaciation (glaciation). (d) AP_{comp} $\Delta\delta^{13}C_{(sub\text{-}deep)}$ (light red from Ziegler *et al.*, 2013; dark orange from this study). (e) AP_{comp} Sortable Silt flow speed record (Starr *et al., 2025*). (f) Source–site temperature gradient from the Dome Fuji ice core (Uemura et al., 2018). (f) ODP Site 1094 Ba/Fe ratio, representing productivity in the Antarctic Zone (Jaccard et al., 2013). Vertical lines indicate Terminations (labelling follows Hodell et al., 2023); dashed lines represent terminations not captured by the AP_{comp} $\Delta\delta^{13}C_{(sub\text{-}deep)}$ record.

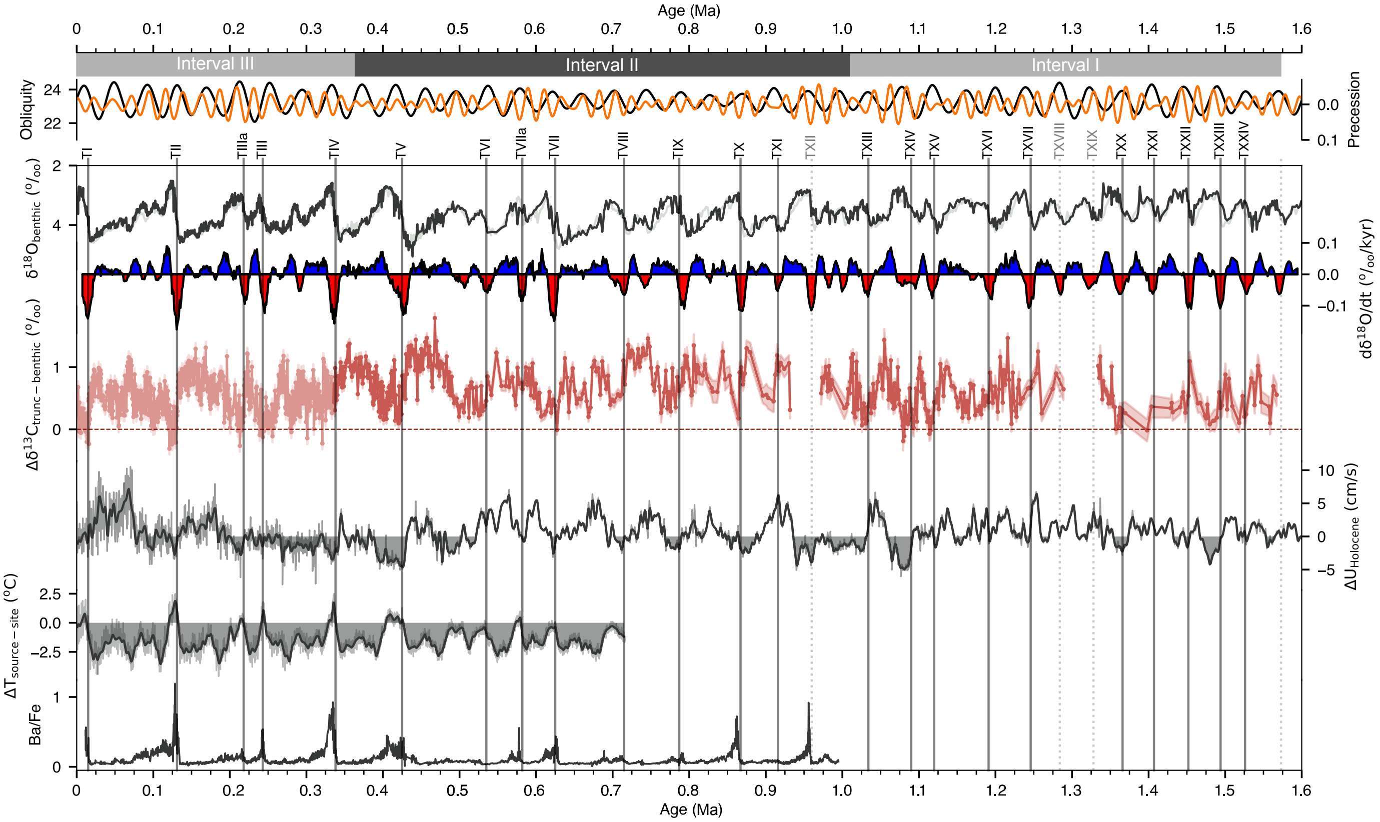

Figure 5. Glacial $\Delta\delta^{13}C_{(sub\text{-}deep)}$. (a) Maximum intensity values for $\Delta\delta^{13}C_{(sub\text{-}deep)}$ (representative MIS values for even-numbered isotope stages). (b) Average $\Delta\delta^{13}C_{(sub\text{-}deep)}$ values for even-numbered isotope stages. Standard error from bootstrap and Gaussian resampling (see text). The three intervals described in the text are shaded.

(a) Glacial Intensity

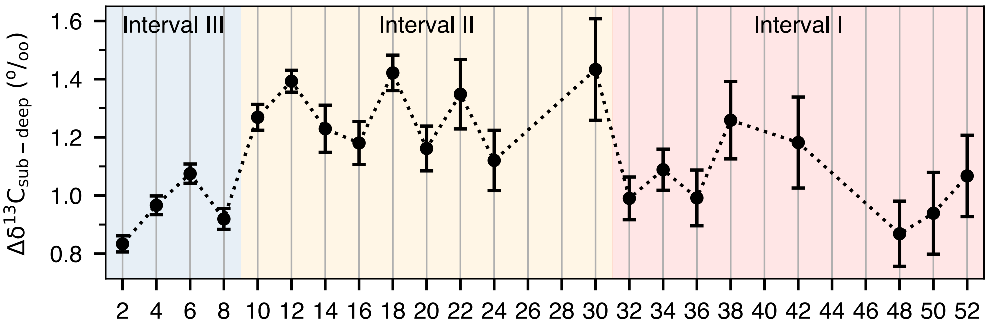

(b) Glacial Average

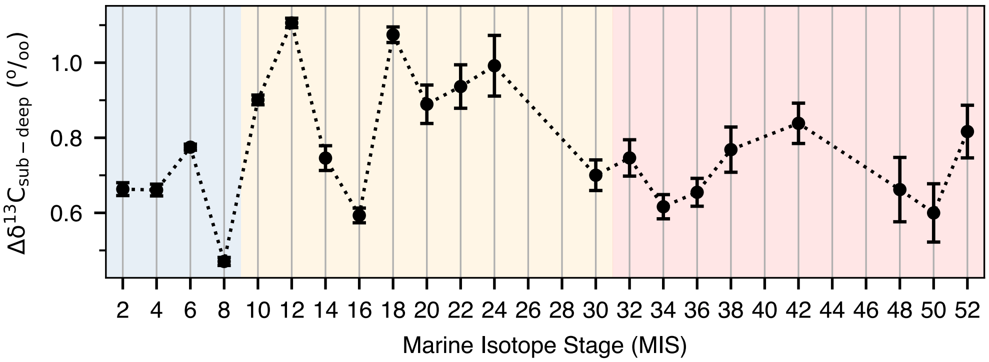

Figure 6. Marine Isotope Stage values for $\Delta\delta^{13}C_{(sub\text{-}deep)}$ versus CO_2 and SAZ Fe accumulation. (a) Comparison of interglacial values for $\Delta\delta^{13}C_{(sub\text{-}deep)}$ (this study) and CO_2 (ice core and boron isotope proxy reconstructions). (b) Same but for glacial stages. The vertical grey shading represents the proposed lower limit for glacial CO_2 (Galbraith & Eggleston, 2017). (c) Same as (a), but for $\Delta\delta^{13}C_{(sub\text{-}deep)}$ versus ODP 1090 Fe accumulation (Martínez-Garcia et al., 2011). (d) Same as (c) but for glacial stages. Linear trends are shown using robust linear regression fits. Shaded regions represent ±1 standard deviation confidence intervals around the regression line, derived from bootstrap resampling iterations implemented via the Seaborn Python package (Waskom, 2021). These intervals reflect uncertainty in the estimated slope and intercept. For suplots (b) and (d), the regression lines only include glacials ≥MIS 10.

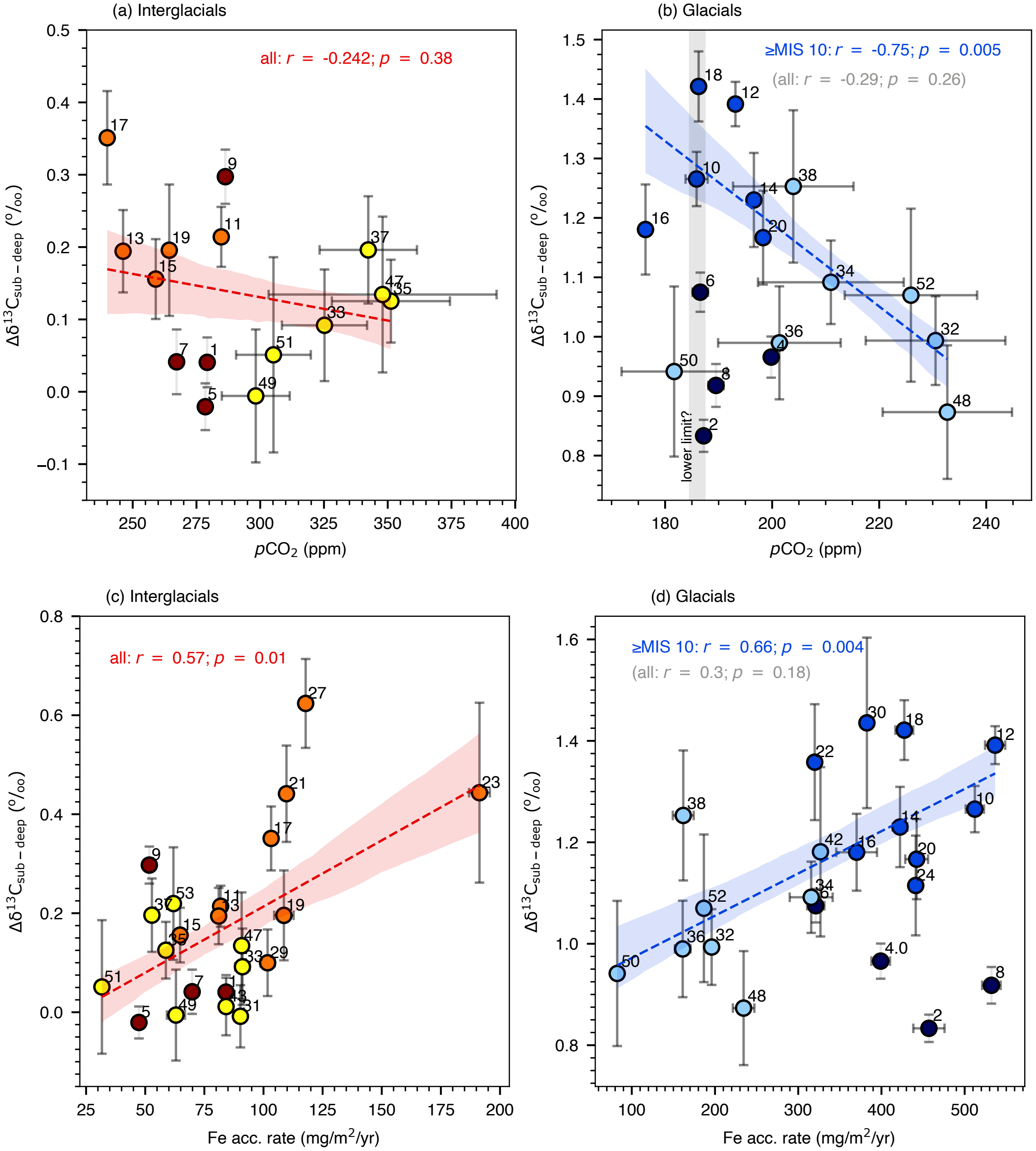

Figure 7. Effect of expansion/contraction of the Subantarctic Zone (SAZ) on APcomp isotope gradients. (a) $\Delta\delta^{13}C_{(sub\text{-}deep)}$ versus $\Delta\delta^{18}O_{(sub\text{-}deep)}$ along a north-south transect of the modern ocean between 20ºE and 30ºE. $\Delta\delta^{13}C_{(sub\text{-}deep)}$ is taken from Suess-corrected $\delta^{13}C$ of Dissolved Inorganic Carbon data at the 400 and 3000m depth levels in the climatology of (Eide et al., 2017). $\Delta\delta^{18}O_{(sub\text{-}deep)}$ is taken from predicted $\delta^{18}O$ of calcite (at equilibrium) at the 400 and 3000m depth levels. Predicted $\delta^{18}O$ of equilibrium calcite is calculated from World Ocean Atlas 2018 temperature data (Locarnini et al., 2018) and gridded $\delta^{18}O$ of seawater data (LeGrande & Schmidt, 2006) using an equation for predicted fractionation in foraminifera (Marchitto et al., 2014). Each marker represents a data point along the north-south transect (color corresponds to latitude), with the position of the AP_{comp} indicted by a red circle. (b) The inset axis (b) shows the evolution of our proxy $\Delta\delta^{13}C_{(sub\text{-}deep)}$ and $\Delta\delta^{18}O_{(sub\text{-}deep)}$ reconstructions between the three key time intervals outlined in the text. (c) Shows the relative change in $\Delta\delta^{13}C_{(sub\text{-}deep)}$ expected from an equatorward expansion (negative shift) or poleward contraction (positive shift) in the SAZ extent. (d) Same as (c) but for the relative change in $\Delta\delta^{18}O_{(sub\text{-}deep)}$.